MIT Libraries | DSpace@MIT

MIT Open Access Articles

IL-33 Signaling Alters Regulatory T Cell Diversity in Support of Tumor Development

The MIT Faculty has made this article openly available. ***Please share*** how this access benefits you. Your story matters.

Citation: Li, Amy et al. "IL-33 Signaling Alters Regulatory T Cell Diversity in Support of Tumor Development." Cell Reports 29, 10 (December 2019): P2998-3008.e8 © 2019 The Author(s)

As Published: http://dx.doi.org/10.1016/j.celrep.2019.10.120

Publisher: Elsevier BV

Persistent URL: https://hdl.handle.net/1721.1/126003

Version: Final published version: final published article, as it appeared in a journal, conference proceedings, or other formally published context

Terms of use: Creative Commons Attribution 4.0 International license

Massachusetts Institute of Technology

Report

Cell Reports

IL-33 Signaling Alters Regulatory T Cell Diversity in Support of Tumor Development

Graphical Abstract

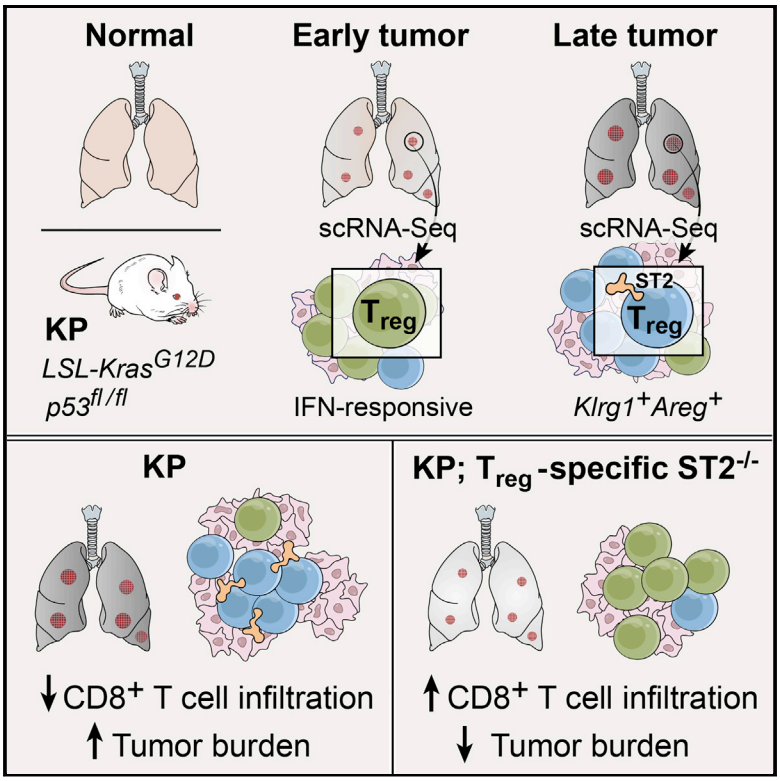

Highlights

- Single-cell profiling of CD4 T cells along tumor development in a mouse model
- T_{reg} diversity shifts to a *Klrg1*$^{+}$*Areg*$^{+}$ (KA) effector phenotype in advanced tumors
- *Il1rl1* (encoding ST2)$^{+}$ T_{regs} have higher expression of KA effector T_{reg} genes
- T_{reg}-specific ST2 loss enhances CD8^{+} T cell infiltration and decreases tumor burden

Authors

Amy Li, Rebecca H. Herbst, David Canner, ..., Michael Birnbaum, Aviv Regev, Tyler Jacks

Correspondence

aregev@broadinstitute.org (A.R.), tjacks@mit.edu (T.J.)

In Brief

Li et al. show in a genetic mouse model of lung adenocarcinoma that during tumor development regulatory T cell (T_{reg}) diversity shifts from an interferon-responsive to a ST2-positive, *Klrg1*$^{+}$*Areg*$^{+}$ effector-like phenotype. T_{reg}-specific deletion of ST2 alters T_{reg} heterogeneity, increases tumor infiltration by CD8^{+} T cells, and decreases tumor burden.

Li et al., 2019, Cell Reports *29*, 2998–3008
December 3, 2019 © 2019 The Author(s).
https://doi.org/10.1016/j.celrep.2019.10.120

OPEN ACCESS
CellPress

Cell Reports
Report

IL-33 Signaling Alters Regulatory T Cell Diversity in Support of Tumor Development

Amy Li,[1,2,3,10] Rebecca H. Herbst,[3,4,10] David Canner,[1,2,10] Jason M. Schenkel,[1,5] Olivia C. Smith,[1] Jonathan Y. Kim,[1] Michelle Hillman,[1] Arjun Bhutkar,[1] Michael S. Cuoco,[4] C. Garrett Rappazzo,[1,9] Patricia Rogers,[4] Celeste Dang,[1] Livnat Jerby-Arnon,[4] Orit Rozenblatt-Rosen,[4] Le Cong,[6,7] Michael Birnbaum,[1,9] Aviv Regev,[1,2,4,8,*] and Tyler Jacks[1,2,8,11,*]
[1]David H. Koch Institute for Integrative Cancer Research, Massachusetts Institute of Technology, 500 Main Street, Cambridge, MA 02139, USA
[2]Department of Biology, Massachusetts Institute of Technology, 77 Massachusetts Avenue, Cambridge, MA 02139, USA
[3]Harvard Medical School, 25 Shattuck Street, Boston, MA 02115, USA
[4]Broad Institute of MIT and Harvard, 415 Main Street, Cambridge, MA 02142, USA
[5]Department of Pathology, Brigham and Women's Hospital, Boston, MA 02115, USA
[6]Department of Pathology, Stanford University, Stanford, CA 94305, USA
[7]Department of Genetics, Stanford University, Stanford, CA 94305, USA
[8]Howard Hughes Medical Institute, Massachusetts Institute of Technology, Cambridge, MA 02139, USA
[9]Department of Biological Engineering, Massachusetts Institute of Technology, 21 Ames Street, Cambridge, MA 02142, USA
[10]These authors contributed equally
[11]Lead Contact
*Correspondence: aregev@broadinstitute.org (A.R.), tjacks@mit.edu (T.J.)
https://doi.org/10.1016/j.celrep.2019.10.120

SUMMARY

Regulatory T cells (T_{regs}) can impair anti-tumor immune responses and are associated with poor prognosis in multiple cancer types. T_{regs} in human tumors span diverse transcriptional states distinct from those of peripheral T_{regs}, but their contribution to tumor development remains unknown. Here, we use single-cell RNA sequencing (RNA-seq) to longitudinally profile dynamic shifts in the distribution of T_{regs} in a genetically engineered mouse model of lung adenocarcinoma. In this model, interferon-responsive T_{regs} are more prevalent early in tumor development, whereas a specialized effector phenotype characterized by enhanced expression of the interleukin-33 receptor ST2 is predominant in advanced disease. T_{reg}-specific deletion of ST2 alters the evolution of effector T_{reg} diversity, increases infiltration of $CD8^+$ T cells into tumors, and decreases tumor burden. Our study shows that ST2 plays a critical role in T_{reg}-mediated immunosuppression in cancer, highlighting potential paths for therapeutic intervention.

INTRODUCTION

The clinical success of immune checkpoint inhibitors in the treatment of non-small cell lung cancer (NSCLC) highlights how targeting immunosuppression in the tumor microenvironment can be an effective therapeutic strategy (Makkouk and Weiner, 2015; Soria et al., 2015). However, only some patients respond to immune therapies, suggesting that an improved understanding of other immunosuppressive mechanisms is needed for effective treatment.

One major mechanism of immunosuppression is posed by $CD4^+$ regulatory T cells (T_{regs}), which can impair anti-tumor immune responses (Tanaka and Sakaguchi, 2017). T_{regs} are critical for maintaining immune tolerance and preventing autoimmunity (Josefowicz et al., 2012). T_{regs} are associated with poor prognosis in several cancers, including lung adenocarcinoma (Shang et al., 2015; Suzuki et al., 2013). In mouse models, T_{reg} depletion can enhance anti-tumor immunity (Bos et al., 2013; Joshi et al., 2015; Marabelle et al., 2013), and antibodies directed against CTLA-4 act in part by depleting T_{regs} (Simpson et al., 2013).

Due to their phenotypic diversity, T_{regs} differentially impact tumor immune responses, such that effector T_{regs} promote tumor growth (Green et al., 2017), whereas poorly immunosuppressive T_{regs} contribute to anti-tumor immunity (Overacre-Delgoffe et al., 2017; Saito et al., 2016). This functional diversity may be reflected in their transcriptional programs. T_{regs} in distinct tissues and inflammatory contexts have transcriptional profiles related to their tissue-resident functions (Panduro et al., 2016). In human tumors, T_{regs} have a program that may be shared across cancer types and is associated with clinical outcome (De Simone et al., 2016; Magnuson et al., 2018; Plitas et al., 2016). Characterization of pro-tumorigenic T_{reg} subsets may guide efforts to target these populations.

Inducible, autochthonous models of cancer are ideal for studying mechanisms of tumor tolerance because they recapitulate the longitudinal development and features of the endogenous tumor microenvironment better than transplanted, more "foreign" tumors (Dranoff, 2011). Our group has previously developed a model of lung adenocarcinoma in which activation of oncogenic *K-ras*^{G12D} and loss of *Trp53* are driven by intratracheal delivery of a lentivirus expressing Cre recombinase (KP: *LSL-Kras*^{G12D}, *p53*$^{fl/fl}$) (DuPage et al., 2009; Jackson et al., 2005). Using a lentivirus that also expresses known T cell

 © 2019 The Author(s).
This is an open access article under the CC BY license (http://creativecommons.org/licenses/by/4.0/).

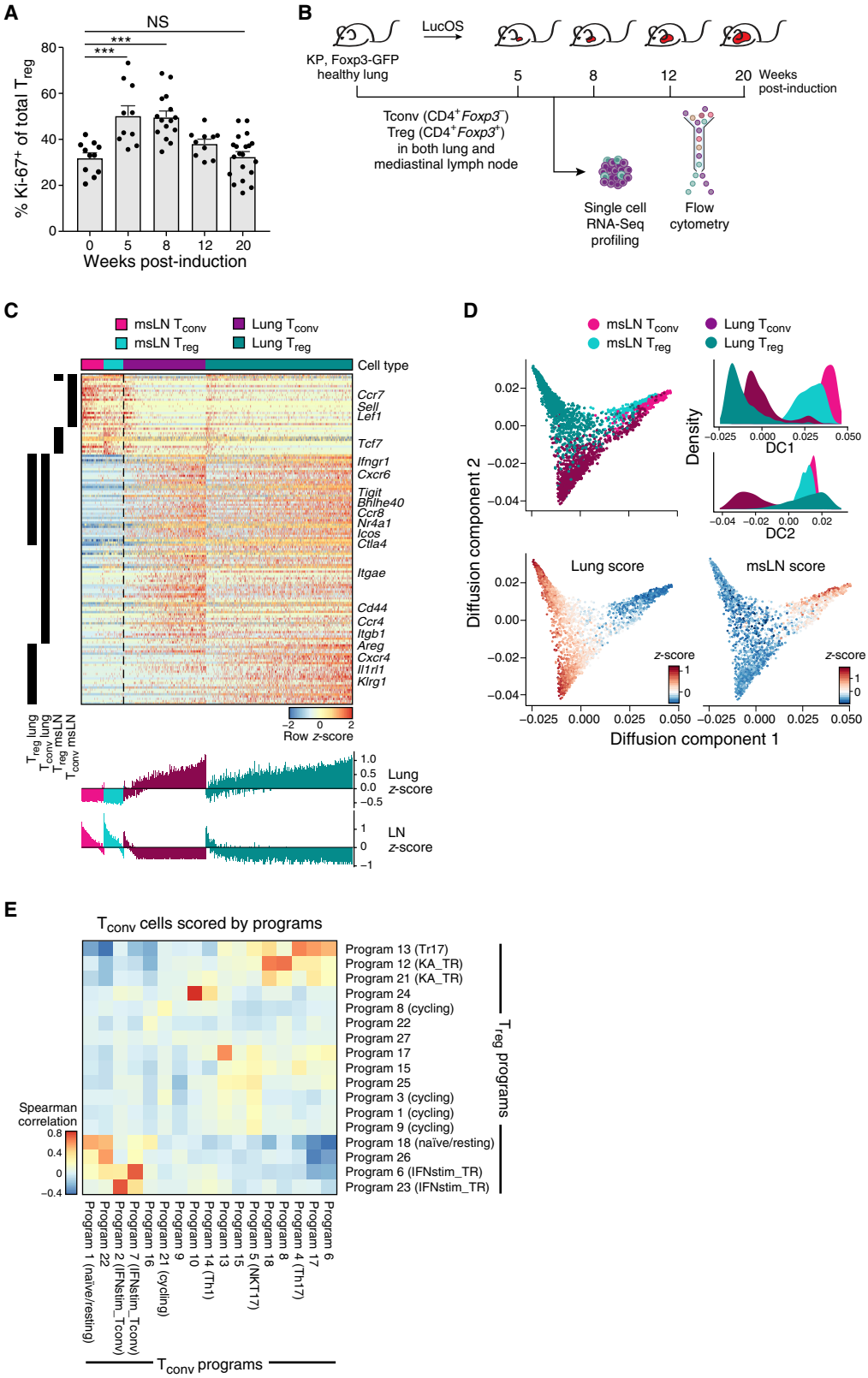

(legend on next page)

antigens (LucOS: luciferase fused to chicken ovalbumin [Ova] and the peptide SIYRYYGL), we can monitor tumor-specific T cell responses (DuPage et al., 2011). T cell infiltration of these tumors delays tumor growth, but the number and activity of anti-tumor CD8$^+$ T cells decline over time, and the development of immune tolerance is partly due to the expansion of lung T_{regs} (Joshi et al., 2015). T_{reg} depletion results in T cell infiltration of tumors, suggesting that T_{regs} actively suppress anti-tumor immune responses. Because T_{reg}-depleted animals succumb to systemic autoimmunity, a strategy targeting features of lung tumor-specific T_{regs} is required to minimize self-directed cytotoxicity.

Here, we map the diversity of conventional CD4$^+$ T cells (T_{convs}) and T_{regs} throughout tumor development in the KP model using single-cell RNA sequencing (scRNA-seq). Whereas T_{conv} subsets were stable over time, T_{reg} diversity changed with tumor progression. At early time points, T_{regs} expressed genes associated with interferon (IFN) signaling, whereas mice with advanced disease had more killer cell lectin-like receptor 1 (*Klrg1*)$^+$ and amphiregulin (*Areg*)$^+$ T_{regs}. Analyzing these data, we identified ST2 as a potential mediator of effector T_{reg} phenotypes during tumor development. T_{reg}-specific ablation of ST2 altered longitudinal patterns of T_{reg} diversity, increased CD8$^+$ T cell infiltration of tumors, and reduced tumor size. Our high-resolution characterization of T_{reg} diversity in the tumor microenvironment thus allows us to refine ways to target T_{reg} function in cancer.

RESULTS

scRNA-Seq Reveals Lung-Specific Transcriptional Programs for Tumor-Associated CD4$^+$ T_{convs} and T_{regs}

Consistent with prior reports that lung T_{regs} expand during KP tumor development (Joshi et al., 2015), the fraction of Ki-67$^+$ T_{regs} by flow cytometry was elevated in lungs with early tumors (Figure 1A), whereas the fraction of Ki-67$^+$ T_{convs} was modestly increased at 5 and 8 weeks but returned to baseline by 12 weeks (Figure S1A).

We hypothesized that this early proliferation of T_{regs} may be associated with changes in T_{reg} diversity. We used scRNA-seq to characterize heterogeneity in tumor-associated CD4$^+$ T cells over time and the relationship between T_{reg} and T_{conv} diversity. We profiled by full-length scRNA-seq 1,254 T_{convs} and 1,679 T_{regs} from the lungs and mediastinal lymph nodes (msLNs) of non-tumor-bearing and tumor-bearing KP, *Foxp3*^{GFP} mice along a time course after tumor induction (Figure 1B).

Tissue-specific programs included both genes shared by lung T_{convs} and T_{regs} and genes uniquely upregulated in each (Figure 1C; Table S1). Lung T_{regs} expressed high levels of *Il1rl1*, *Cxcr4*, *Areg*, and *Klrg1* compared with msLN T_{regs}, whereas T_{convs} expressed *Cd44*, *Ccr4*, and *Itgb1* (Figure 1C). Gene programs associated with a recently described transcriptional trajectory of tissue-resident T_{regs} (Miragaia et al., 2019) were consistent with those highlighted by our scRNA-seq profiles of lung cells (Figure S1B). msLN T_{regs} and T_{convs} expressed genes associated with a naive or central memory phenotype, including *Lef1*, *Sell*, and *Ccr7* (Figures 1C and S1C), whereas lung cells were more activated (Figure 1C). Subsets of lung T_{convs} and T_{regs} that scored high for the msLN signature also expressed genes associated with T cell receptor (TCR) signaling, including *Nr4a1* and *Junb*, suggesting that they may be recently activated (Figure S1C).

Both lung and msLN cells spanned a spectrum of cell states, with lung cells showing higher diversity. This was apparent when lung and msLN signature genes were used to create a diffusion map (Figures 1D and S1D; STAR Methods; Haghverdi et al., 2015).

Lung T_{conv} and T_{reg} Subsets Share a Limited Number of Expression Programs, Including a Th17-like Phenotype

To assess the different transcriptional programs of T_{conv} and T_{reg} subsets in the lung, we performed PAthway and Gene set Over-Dispersion Analysis (PAGODA) (Fan et al., 2016) to identify groups of genes with co-varying expression (STAR Methods; Figures S1E and S1F; Table S2). The relative proportions of cells expressing markers of different T_{conv} programs remained stable during tumor development (Figure S1G). T_{conv} and T_{reg} subsets expressed several overlapping programs, including programs associated with naive/resting T cells and IFN signaling (Figure 1E).

Of the T_{conv} programs associated with effector CD4$^+$ T cell subsets, only the Th17 program was correlated with a T_{reg} program (program 13; Figure 1E). Program 13 marks T_{regs} that express *Rorc* and *Il17a* (Figure S1H), reminiscent of Th17-like effector T_{regs} (Tr17), which are thought to inhibit Th17 responses (Kim et al., 2017). By flow cytometry, RORγt$^+$ T_{regs} comprise ~10% of lung T_{regs} throughout tumor development (Figure S1I). Expression of program 13 and lung T_{reg} signature genes was inversely correlated (Figures S1J and S1K), suggesting that Tr17-like cells represent a distinct state.

Remarkably, TCR clonotypes shared between T_{regs} and T_{convs} were predominantly Tr17-like and Th17-like cells, respectively.

Figure 1. scRNA-Seq Reveals Distinctive Lung CD4$^+$ T Cell Signatures and Overlapping T_{conv} and T_{reg} Diversity

(A) T_{reg} proliferation peaks early in tumor development. Percent Ki-67$^+$ T_{regs} throughout KP tumor development from two to three experiments (dot: one mouse). Error bars: SEM. ***$p < 0.001$, Tukey's multiple comparisons test. NS, non-significant.

(B) Experiment overview. KP, *Foxp3*^{GFP} mice were harvested at the indicated weeks after tumor induction with Lenti-LucOS. 1,254 T_{convs} and 1,679 T_{regs} from lung and msLNs were profiled by plate-based scRNA-seq.

(C) Lung-specific gene expression programs include genes shared by, and unique to, T_{convs} and T_{regs}. Genes (rows, row-normalized) differentially expressed (STAR Methods) between cells from lung versus msLNs for T_{regs} and T_{convs} (columns). Left black bars indicate significantly differentially expressed T_{reg} and T_{conv} genes. Bottom: cell expression scores for corresponding lung and LN signatures. Color indicates cell type and tissue of origin.

(D) Lung cells show particular diversity. Diffusion component (DC) embedding of all cells (dots), colored by cell type and tissue of origin (top left), or *Z* score of the lung (bottom left) or msLN (bottom right) programs. Top right: distribution of DC scores.

(E) Lung T_{regs} and T_{convs} have highly correlated programs. Spearman's correlation coefficient (color bar) of T_{conv} expression *Z* scores for T_{conv} programs (columns) and T_{reg} programs (rows) (STAR Methods).

Twelve TCR clonotypes were shared across T_{regs} and T_{convs} (Table S3; STAR Methods). Of the 19 T_{regs} and 20 T_{convs} belonging to these shared TCR clonotypes, 13 T_{regs} were Tr17-like (Figures S1L and S1M). Due to the small number of identified clonotypic families, no temporal trend could be reliably detected. Overall, this suggests that Tr17 differentiation may reflect a shared clonal origin with Th17 cells.

A *Klrg1*$^+$*Areg*$^+$ Effector-like T_{reg} Program Becomes Predominant during Tumor Development

In contrast with Tr17-like cells, which represented a fixed proportion of lung T_{regs} during tumor development, other T_{reg} programs changed in prominence over time (Figure 2A). After 8 weeks, there was decreased expression of programs 1, 3, 8, and 9, which marked cycling cells (Figure 2A), corresponding to the decline in Ki67$^+$ T_{regs} (Figure 1A). Two other programs also changed over time, reflecting an IFN response (programs 6 and 23; Figures 2A–2C; Figure S2A) and a *Klrg1*$^+$*Areg*$^+$ (KA) effector-like program (programs 12 and 21; Figures 2A–2C; Figures S2A and S2B).

The IFN-responsive T_{reg} program ("IFNstim_TR") included many IFN-stimulated genes (ISGs) downstream of either type I or II IFN signaling. Twenty-eight genes from the IFNstim_TR program were significantly downregulated in T_{regs} during tumor progression (Figure S2C; STAR Methods). IFNγ promotes a T-bet$^+$CXCR3$^+$ T_{reg} population that can suppress Th1 responses (Hall et al., 2012; Koch et al., 2009, 2012). Neither *Cxcr3* nor *Tbx21* are IFNstim_TR genes, but IFNstim_TR expression was correlated with *Tbx21* expression (Figure S2D). Moreover, cells scoring highly for the IFNstim_TR program also scored highly for a lymphoid tissue T_{reg} program (Figure S2E), and msLN T_{regs} had higher expression of IFNstim_TR genes compared with lung T_{regs} at 12 and 20 weeks post induction (p.i.) (Figure S2F). Taken together, T_{regs} expressing the IFN-responsive program ("IR T_{regs}") were most prevalent early in tumor development and in msLNs, and may thus have recently arrived to the lung.

Meanwhile, the *Klrg1*$^+$*Areg*$^+$ effector-like T_{reg} program ("KA_TR") included genes upregulated in T_{regs} from mouse non-lymphoid tissues and human cancers (Figure S2E; STAR Methods). T_{regs} expressing the KA_TR program ("KA T_{regs}") expressed *Ccr6*, but not *Cxcr3*, representing a population distinct from IR T_{regs} (Figure S2G). *Klrg1* and *Areg* expression have been associated with T_{reg} differentiation and tissue repair, respectively (Arpaia et al., 2015; Burzyn et al., 2013; Cheng et al., 2012). 40% of lung T_{regs} from KP mice with advanced disease have been shown to be CD103$^+$KLRG1$^+$ (double-positive [DP]) (Joshi et al., 2015). The KA_TR program was enriched for genes upregulated in DP T_{regs} (Figures S2H and S2I; STAR Methods), including genes associated with T cell activation and putative T_{reg} effector functions (e.g., *Nr4a1*, *Cd69*, *Il1rl1*, *Areg*, *Srgn*, and *Fgl2*). KA and DP T_{regs} are highly similar and are likely representative of a KLRG1$^+$ effector T_{reg} population.

The IR and KA T_{reg} programs represented distinct T_{reg} phenotypes within each time point and followed opposite temporal patterns: expression of IFNstim_TR genes was highest in cells from week 5 and declined thereafter, whereas expression of KA_TR genes increased and remained elevated (Figures 2A–2C). This trend was reflected by individual genes: *Cxcr3* expression decreased, whereas *Pdcd1* and *Lilrb4* expression increased during tumor development (Figure S2J). More generally, KA_TR genes were upregulated in DP T_{regs}, whereas *Cxcr3* and IFNstim_TR genes were significantly downregulated (Figures S2H and S2K). Indeed, CXCR3 protein levels decreased, and proteins encoded by KA_TR genes, including CD85k, CD69, CXCR6, PD-1, and ST2, increased during tumor progression (Figure 2D). Taken together, our data suggest that tumor progression may be associated with a shift from the IR to KA T_{reg} programs. We hypothesize that the immunosuppression associated with late-stage tumors may be because of the prevalence of KA T_{regs}.

ST2 May Promote the KA T_{reg} Phenotype in Mice Bearing Advanced Lung Tumors

Il1rl1, a KA_TR gene that encodes the interleukin-33 (IL-33) receptor ST2, marked a heterogeneous T_{reg} population that had higher expression of KA_TR genes. ST2 was most highly expressed in DP lung T_{regs} (Figure 3A), consistent with prior data that ST2 marks a tissue T_{reg} program that expresses KLRG1 and GATA3 (Delacher et al., 2017). *Il1rl1*$^+$ and *Il1rl1*$^-$ T_{regs} both spanned a full spectrum of cell states (Figure S3A) and had similar transcriptional diversity (Figure S3B; STAR Methods). Nevertheless, *Il1rl1*$^+$ T_{regs} had higher expression of KA_TR and DP genes and lower expression of Th17-like and resting T_{reg} genes (Figures 3B, S3C, and S3D). *Il1rl1*$^+$ T_{regs} also had lower expression of IFNstim_TR genes compared with *Il1rl1*$^-$ T_{regs} in non-tumor-bearing lungs (Figure S3C). *Il1rl1*$^+$ and *Il1rl1*$^-$ T_{regs} had similar expression of cell-cycle genes and Ki-67 (Figures S3C and S3E), suggesting that proliferation does not account for the observed differences in phenotype. Genes differentially expressed between *Il1rl1*$^+$ and *Il1rl1*$^-$ T_{regs} from human colon cancer were also enriched for KA_TR genes (Figure 3C; STAR Methods). ST2 signaling may thus be a conserved pathway in human and mouse T_{regs} that promotes the KA/DP T_{reg} phenotype and/or the proliferation of KA/DP T_{regs}. Consistent with the presence of ST2 signaling throughout tumor development, IL-33, the only known ligand of ST2, was highly expressed in normal lung and in early and late KP tumors (Figure 3D). IL-33 was predominantly expressed on surfactant protein C (SPC$^+$) type II epithelial (AT2) cells in normal lung (Figure S3F), and AT2 and mesenchymal cells in tumor-bearing lungs (Figure S3G), consistent with prior reports (Treutlein et al., 2014).

ST2 protein was preferentially expressed by lung T_{regs} late in tumor development. ST2 levels on lung T_{regs} increased with time (Figure 2D), and ST2 was expressed primarily by T_{regs}, with lower expression in CD8$^+$ T cells and T_{convs} (Figures 3E and S3H). We hypothesized that the expansion of ST2$^+$ T_{regs} may drive the increase in KA/DP T_{regs} during lung tumor development.

T_{reg}-Specific ST2 Is Required for the Increase in DP T_{regs} during Tumor Progression

To test whether ST2 signaling was necessary to develop the KA/DP T_{reg} response, we studied the effects of T_{reg}-specific *Il1rl1* deletion. We used a modified KP model, where FlpO recombinase induces expression of oncogenic K-ras and loss of p53 (KPfrt: *FSF-Kras*^{G12D}, *p53*$^{frt/frt}$) (Lee et al., 2012), allowing us to use the Cre-lox system to delete *Il1rl1* in T_{regs}. We crossed KPfrt and *Foxp3*$^{YFP\text{-}Cre}$, *Il1rl1*$^{fl/fl}$ mice to model lung adenocarcinoma in

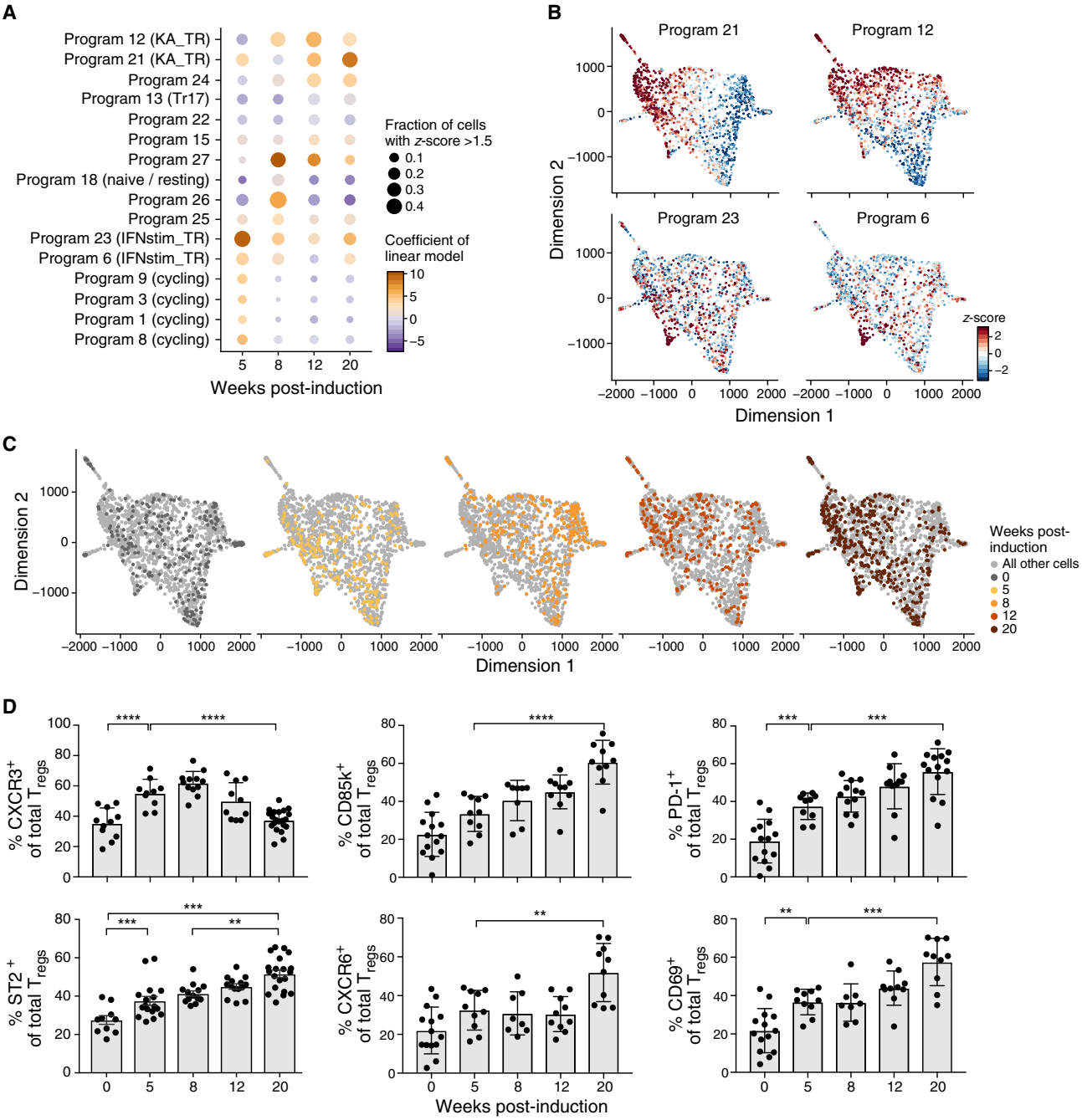

Figure 2. A *Klrg1*$^+$*Areg*$^+$ T_{reg} Phenotype Becomes Dominant during Tumor Development

(A) Changes in prominence of cycling, IFN-stimulated, and T_{reg} effector-like programs with tumor development. Linear regression analysis of program expression *Z* scores as a function of time since tumor initiation. Dot plot shows for each program (row) and time point (column) the coefficient of the time point covariate (color scale) with non-tumor-bearing lung as reference and the percentage of cells with *Z* score > 1.5 (dot size).

(B and C) An IFN and a *Klrg1*$^+$*Areg*$^+$ effector-like program peak early and late in tumor development, respectively. Two-dimensional force-directed layout embedding of lung T_{regs} colored by normalized program *Z* score for the KA_TR program (B, top, programs 12 and 21), IFNstim_TR program (B, bottom, programs 6 and 23), and time point (C).

(D) Percentage of T_{regs} expressing the indicated protein (y axis) throughout KP tumor development (x axis) from two to three experiments (dot: one mouse). Error bars: SEM. **p < 0.01, ***p < 0.001, ****p < 0.0001, Tukey's multiple comparisons test.

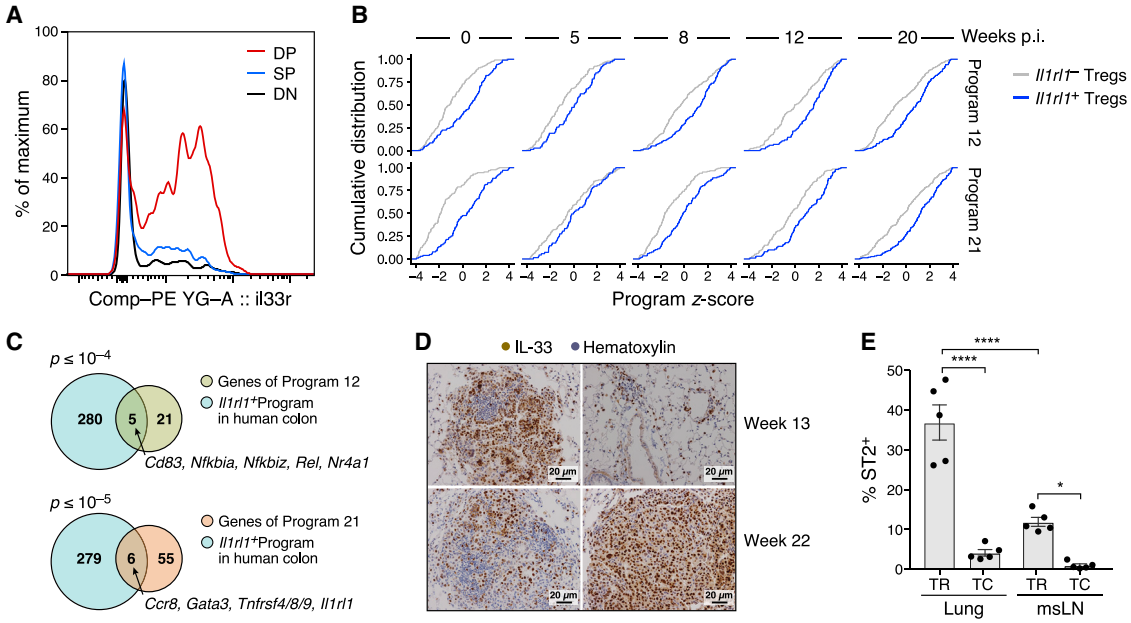

Figure 3. ST2 Marks a Diverse Population of KA/DP T_{regs} in Lung Tumor-Bearing Mice

(A) ST2 is most highly expressed in DP lung T_{regs}. Representative distributions of ST2 expression on CD103$^-$KLRG1$^-$ (DN, gray), CD103$^+$KLRG1$^-$ (SP, blue), and CD103$^+$KLRG1$^+$ (DP, red) T_{regs} isolated from tumor-bearing lungs.

(B) KA_TR genes are upregulated in *Il1rl1*$^+$ T_{regs} throughout tumor development. Empirical cumulative distribution functions (ECDFs) of the scores of programs 12 (top) and 21 (bottom) of *Il1rl1*$^+$ (blue) versus *Il1rl1*$^-$ T_{regs} (gray) by time point after tumor induction.

(C) *Il1rl1*$^+$ T_{regs} in human colon cancer have higher expression of KA_TR genes. Overlap of genes upregulated in *Il1rl1*$^+$ T_{regs} in human colon cancer (blue) and programs 12 (top, $p = 1.5 \times 10^{-5}$) and 21 (bottom, $p = 5.3 \times 10^{-6}$) genes (STAR Methods). p values: hypergeometric test.

(D) IL-33 is highly expressed in lung adenocarcinoma. Immunohistochemistry (IHC) staining of tumor-bearing lungs from KP mice at weeks 13 and 22 p.i. with Lenti-LucOS. Two representative images are shown per time point. Scale bar: 20μm.

(E) Lung T_{regs} are enriched for ST2$^+$ cells in late-stage tumors. Percent ST2$^+$ among lung and msLN T_{regs} and T_{convs} from tumor-bearing KP mice at week 20 p.i. as measured by flow cytometry. Error bars: SEM. ****$p < 0.0001$, *$p < 0.05$, Tukey's multiple comparisons test.

the setting of T_{reg}-specific ST2 deficiency (Figure 4A). We infected the mice with a lentivirus expressing FlpO recombinase and GFP fused to Ova and SIYRGYYL (FlpO-GFP-OS) in order to induce tumors that would express the same T cell antigens as those in the LucOS model. Confirming T_{reg}-specific recombination of the *Il1rl1* locus, ST2 expression was unchanged in CD8$^+$ T cells and T_{convs} (Figure S4A).

Early-stage KPfrt, *Foxp3*$^{YFP\text{-}Cre}$, *Il1rl1*$^{fl/fl}$ (KPF-ST2^{FL}) and KPfrt, *Foxp3*$^{YFP\text{-}Cre}$ (KPF) mice had similar fractions of T_{convs} and T_{regs} (Figure S4B), but late in tumor progression KPF-ST2^{FL} mice had a lower proportion of T_{regs}, of which fewer were DP T_{regs} (Figures 4B and 4C). Notably, DP T_{regs} from KPF and KPF-ST2^{FL} mice had similar Ki-67 expression, suggesting that the decreased fraction of DP T_{regs} in KPF-ST2^{FL} mice was not due to impaired proliferation (Figure S4C). msLNs and splenic T_{regs} did not have fewer DP T_{regs} (Figure S4D). Proportions of Th1, Th17, CD8$^+$ T cells, tumor antigen-specific CD8$^+$ T cells, and alveolar macrophages were also comparable among KPF-ST2^{FL} mice and controls (Figures S4E–S4H).

Bulk RNA-seq of DP, single-positive (SP), and double-negative (DN) T_{regs} from KPF-ST2^{FL} and KPF mice identified an expression signature lower in KPF-ST2^{FL} versus KPF T_{regs} and highest among KPF DP T_{regs} (Figures 4D and S4I). The signature was enriched for DP signature genes, including *Dgat2*, *Furin*, and *Nfkbia*, genes preferentially expressed in *Il1rl1*$^+$ T_{regs} ($p = 1.2 \times 10^{-13}$, hypergeometric test) and genes upregulated by T_{regs} in human NSCLC (Figures S4J and S4K). KPF-ST2^{FL} T_{regs} also showed higher expression of some genes, including *Itgb1*, *Il10*, *Klf6*, and *Fos* (Figure 4D), suggesting that they may adopt alternative phenotypes.

We hypothesized that KPF-ST2^{FL} mice may have altered proportions of Tr17-like and CXCR3$^+$ T_{regs}. Indeed, CXCR3$^+$CCR6$^-$ T_{regs} were increased, whereas CXCR3$^-$CCR6$^+$ T_{regs} were decreased, in KPF-ST2^{FL} mice compared with KPF mice (Figures 4E and S4L). However, RORγt expression was unchanged (Figure S4M), suggesting that a CCR6$^+$ T_{reg} population exclusive of Tr17-like cells decreases in KPF-ST2^{FL} mice. Earlier in tumor development, CXCR3$^+$ T_{regs} from KPF-ST2^{FL} mice also had increased fluorescence intensity of CXCR3 (Figure S4N). Taken together, our data support the hypothesis that ST2 regulates T_{reg} diversity over time by promoting the KA/DP T_{regs} over alternate phenotypes.

T_{reg}-Specific ST2 Ablation Leads to Increased CD8$^+$ T Cell Infiltration and a Reduction in Tumor Burden

Tumors from KPF-ST2^{FL} mice had >50% higher CD8$^+$ T cell infiltration than tumors from KPF mice, resulting in higher CD8/T_{reg} ratios (Figure 4F). KPF-ST2^{FL} mice also had a lower tumor burden and smaller tumors compared with controls (Figures 4G and S4O), suggesting that greater CD8$^+$ T cell infiltration of

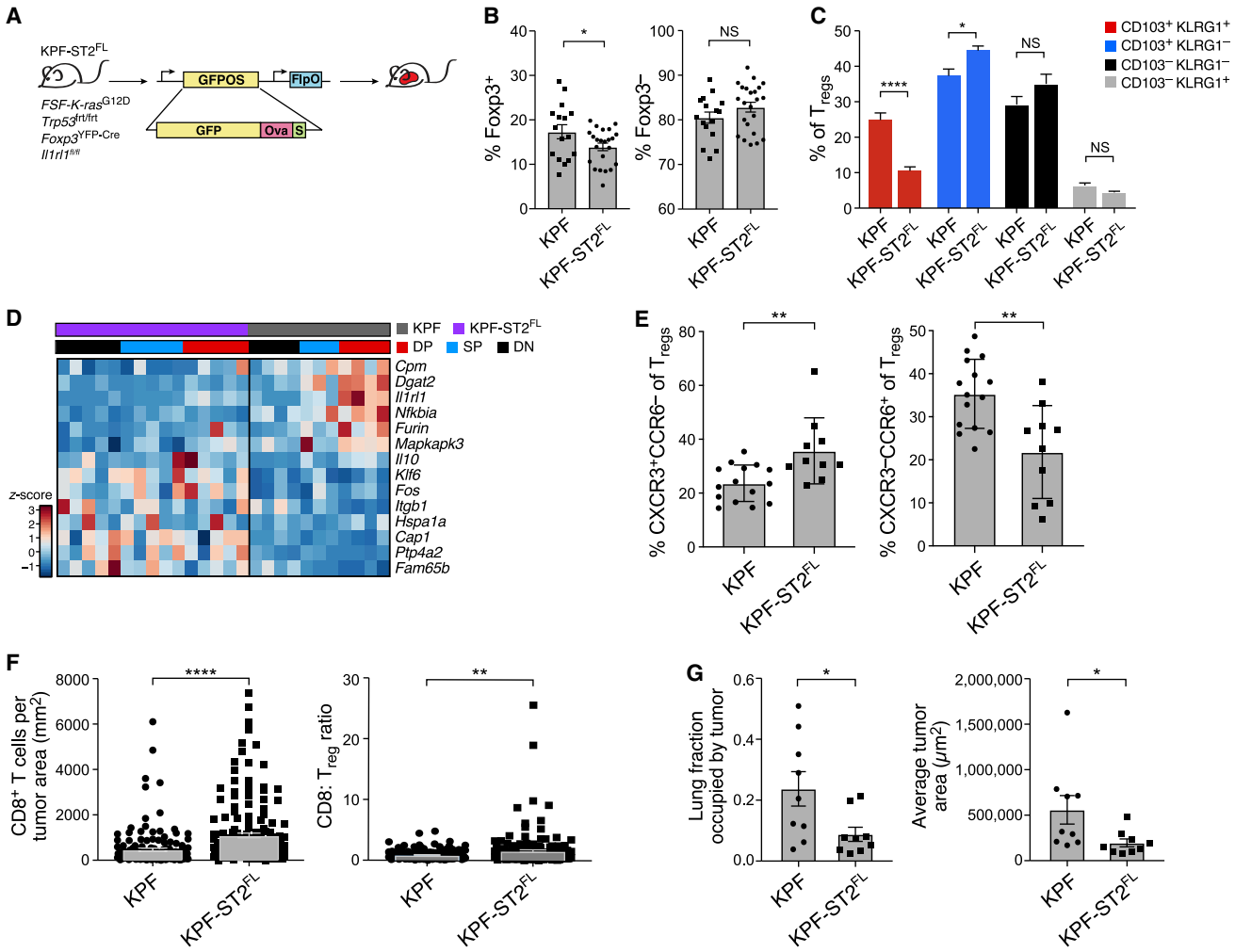

Figure 4. T_{reg}-Specific ST2 Ablation Alters T_{reg} Diversity and Enhances $CD8^+$ T Cell Infiltration of Tumors

(A) Experiment overview. KPF and KPF-$ST2^{FL}$ mice were infected with FlpO-GFP-OS.

(B, C, and E) Flow cytometric analyses of KPF-$ST2^{FL}$ and KPF mice at 24–25 weeks p.i. All data are from two to three experiments; n = 3–5 mice per group. Error bars: SEM.

(B) Percent T_{regs} (left) and T_{convs} (right) of $CD4^+$ lung cells. *$p < 0.05$, two-tailed Student's t test.

(C) Percent $CD103^-KLRG1^+$ (gray), DN (black), SP (blue), and DP (red) of T_{regs}. ****$p < 0.0001$, *$p < 0.05$, Sidak's multiple comparisons test.

(D) Bulk RNA-seq identifies expression signature distinguishing KPF from KPF-$ST2^{FL}$ T_{regs} from tumor-bearing mice. Row-normalized expression (*Z* score) of select signature genes (rows, STAR Methods) across T_{reg} populations (columns, colored as in C).

(E) Percent $CXCR3^+CCR6^-$ (left) and $CXCR3^-CCR6^+$ (right) of T_{regs}. **$p < 0.01$, two-tailed Student's t test.

(F) Increased $CD8^+$ T cell infiltration in KPF-$ST2^{FL}$ mice. $CD8^+$ cells per tumor area (left) and $CD8/T_{reg}$ ratio (right) in pooled tumors from KPF-$ST2^{FL}$ and KPF mice as measured by immunohistochemistry (IHC) staining of cross sections of tumor-bearing lungs. Error bars: SEM. **$p < 0.01$, ****$p < 0.0001$, Mann-Whitney test.

(G) Reduced tumor burden in KPF-$ST2^{FL}$ mice. Percent of total lung occupied by tumor (left, $p = 0.0315$) and average tumor size (right, $p = 0.0106$) in KPF-$ST2^{FL}$ and KPF mice. Error bars: SEM. Mann-Whitney test was used.

NS, non-significant.

tumors may result in better inhibition of tumor growth. Moreover, tumor infiltration by $Foxp3^+$ T cells was also greater in KPF-$ST2^{FL}$ mice (Figure S4P), supporting the hypothesis that loss of ST2 signaling encourages a pro-inflammatory T_{reg} phenotype rather than reducing T_{reg} numbers. Overall, our study suggests that T_{reg}-specific inhibition of ST2 signaling may result in a less immunosuppressive tumor microenvironment characterized by increased anti-tumor $CD8^+$ T cell activity and lower tumor burden.

DISCUSSION

Mice with T_{reg}-specific ST2 deficiency have impaired growth of transplanted and chronic inflammation-associated tumors (Ameri et al., 2019; Magnuson et al., 2018; Pastille et al., 2019). We show in an autochthonous mouse model of oncogene-driven lung adenocarcinoma that T_{reg}-specific ST2 loss altered T_{reg} diversity and increased $CD8^+$ T cell infiltration, suggesting that KA T_{regs} curb anti-tumor $CD8^+$ T cell activity. Lung $CD8^+$ T cells

express low levels of ST2, suggesting that the observed phenotype is not due to increased ST2 signaling in $CD8^+$ T cells. Indeed, the proportion and phenotype of $CD8^+$ T cells in KPF-$ST2^{FL}$ mice are similar to that of control mice (data not shown). Our data point to the potential value of disrupting ST2 signaling in cancer, especially in concert with other immunotherapies that improve $CD8^+$ T cell function.

We observed a slight reduction in lung T_{regs} in KPF-$ST2^{FL}$ mice, consistent with reports that IL-33 can stimulate TCR-independent expansion of T_{regs} (Arpaia et al., 2015; Kolodin et al., 2015). However, we did not find differences in proliferation between T_{regs} from KPF-$ST2^{FL}$ mice and controls. Instead, ST2-deficient T_{regs} may adopt multiple alternate states because of loss of IL-33 signaling. In contrast with a recent report that colon $ST2^+$ T_{regs} have lower expression of Th17-associated genes, and that recombinant IL-33 inhibits Tr17 differentiation (Pastille et al., 2019), KPF-$ST2^{FL}$ mice did not have a greater proportion of $ROR\gamma t^+$ or IL-17^+ T_{regs}. Rather, loss of IL-33 signaling favored a $CXCR3^+$ phenotype, and DP T_{regs} from KPF-$ST2^{FL}$ mice had lower expression of DP genes, suggesting that ST2 may help regulate the KA/DP T_{reg} phenotype. IL-33 has been shown to increase expression of Foxp3 and GATA-3 (Kolodin et al., 2015; Vasanthakumar et al., 2015), transcription factors critical for T_{reg} differentiation. KA/DP T_{regs} have similar features to previously described "tissue-protective" T_{regs} in muscle, lung, and tumors (Arpaia et al., 2015; Burzyn et al., 2013; Green et al., 2017), providing a basis for how ST2-mediated promotion of these T_{regs} may aid tumor growth. Indeed, KA/DP T_{regs} express a program similar to that of T_{regs} in human cancers (De Simone et al., 2016; Guo et al., 2018), including *TNFRSF9*$^+$ T_{regs} in human NSCLC (Zheng et al., 2017).

CXCR3 directs T_{regs} to sites of Th1 inflammation (Koch et al., 2009), which may explain the prominence of the IFNstim_TR program during early tumorigenesis at the peak of $CD8^+$ T cell tumor infiltration and IFN signaling (DuPage et al., 2011). CXCR3 may mark recently arrived T_{regs} that have distinct functions from KA T_{regs}, and temporal shifts in IFNstim_TR and KA_TR gene expression may reflect T_{reg} adaptation to the tumor microenvironment over time. Alternatively, the decline in $CXCR3^+$ T_{regs} during tumor development may reflect cellular turnover and/or outgrowth of KA T_{regs} because of reduced IFN even as IL-33 remains abundant. Increased expression of CXCR3 in T_{regs} in KPF-$ST2^{FL}$ mice compared with controls suggests that loss of IL-33 signaling results in greater IFN signaling, which is likely associated with enhanced infiltration of tumors by $CD8^+$ T cells, a major source of IFNγ (data not shown). Differential expression of CXCR3 and CCR6 also suggests that T_{reg} localization may be altered in KPF-$ST2^{FL}$ mice, consistent with greater $Foxp3^+$ cell infiltration observed in their tumors. Several reports have described an IFN signature or a distinct population of $CXCR3^+$ T_{regs} in human tumors, although their significance is not well defined (Halim et al., 2017; Johdi et al., 2017; Redjimi et al., 2012).

Longitudinal scRNA-seq in the KP model provides a window into the natural history of T_{conv} and T_{reg} diversity in cancer that is challenging to achieve using bulk populations or patient samples. Tr17-like, IFN-responsive, and KA/DP effector T_{reg} populations have been described previously in human tumors, and we show that these states exist simultaneously and their relative proportions vary with tumor development and ST2 activity. Moreover, loss of ST2 signaling in T_{regs} can alter T_{reg} composition and ultimately impact tumor growth. Although T_{reg} transcriptional heterogeneity may pose a challenge for targeting tumor T_{reg} activity, our study provides proof of concept that pathways that control T_{reg} diversity, maturation, and function may be useful targets for future therapies.

STAR★METHODS

Detailed methods are provided in the online version of this paper and include the following:

- KEY RESOURCES TABLE
- LEAD CONTACT AND MATERIALS AVAILABILITY
- EXPERIMENTAL MODEL AND SUBJECT DETAILS
  - Mice
- METHOD DETAILS
  - Mouse studies
  - Lentiviral production and tumor induction
  - Tissue isolation and preparation of single cell suspensions
  - Staining for flow cytometric analysis
  - Isolation of T_{reg} populations for bulk RNA-Seq
  - Single-cell sorting of T_{conv} and T_{reg} populations for RNA sequencing
  - Droplet-based scRNA-seq of $CD45^+$ and $CD45^-$ populations from tumor-bearing lungs
  - Preparation of scRNaseq libraries
  - Quantitative PCR for validation of RNA-Seq experiments
  - Immunohistochemistry (IHC) and immunofluorescence staining
- QUANTIFICATION AND STATISTICAL ANALYSIS
  - Bulk RNA-seq data pre-processing
  - Signature analysis in bulk RNA-Seq
  - DP T_{reg} signature
  - ST2-deficient T_{regs} Signature
  - Gene Set Enrichment Analysis (GSEA)
  - Pre-processing of SMART-Seq2 scRNA-seq data
  - Identifying tissue-specific gene programs for T_{reg} and T_{conv}
  - Comparing the extent of cell heterogeneity between lung and msLN
  - Identifying gene programs and their time dependence
  - Dimensionality reduction using diffusion component analysis
  - Testing for differential gene expression during tumor development
  - T cell receptor (TCR) reconstruction and clonotype calling
  - Comparison of bulk and scRNA-seq signatures to published signatures
  - ST2 transcriptional programs in human colorectal cancer T_{regs}
  - Processing and analysis of droplet-based scRNA-seq

- Analysis of IHC Images
- Additional statistical analyses
- DATA AND CODE AVAILABILITY

SUPPLEMENTAL INFORMATION

Supplemental Information can be found online at https://doi.org/10.1016/j.celrep.2019.10.120.

ACKNOWLEDGMENTS

We thank N. Joshi, N. Marjanovic, R. Satija, D. Gennert, C. Jin, and S. Riesenfeld for thoughtful discussion and technical advice; J. Park, J. Wilson, and N. Cheng for technical assistance; S. Levine at the Massachusetts Institute of Technology (MIT) BioMicro Center for sequencing support; C. Otis and S. Saldi in the Broad Flow Cytometry Core and G. Paradis in the Koch Institute Flow Cytometry Facility for flow cytometry assistance; K. Cormier and C. Condon from the Hope Babette Tang (1983) Histology Facility for histology assistance; L. Gaffney and A. Hupalowska for artwork and advice on figures; A. Sharpe for *Foxp3*^{GFP} mice; D. Mathis for critical reading of the manuscript and *Il1rl1*$^{fl/fl}$ mice; and K. Anderson, J. Teixeira, M. Magendantz, and K. Yee for administrative and logistical support. This work was supported by the Howard Hughes Medical Institute (T.J. and A.R.), a Margaret A. Cunningham Immune Mechanisms in Cancer Research Fellowship Award (A.L.), the David H. Koch Graduate Fellowship Fund (A.L.), National Cancer Institute (NCI) Cancer Center Support Grant P30-CA1405, an Advanced Medical Research Foundation grant (D.C.), a Cancer Research Institute (CRI) Irvington Postdoctoral Fellowship (L.C.), a National Science Foundation Graduate Fellowship (D.C.), grants T32GM007753 (A.L.) and T32GM007287 (A.L. and D.C.) from the National Institute of General Medical Sciences (NIGMS), and the Klarman Cell Observatory at the Broad Institute (A.R.). A.R. and T.J. are Howard Hughes Medical Institute Investigators. T.J. is the David H. Koch Professor of Biology and a Daniel K. Ludwig Scholar.

AUTHOR CONTRIBUTIONS

A.L., R.H.H., D.C., J.M.S., L.C., A.R., and T.J. designed the study. A.L., D.C., and J.M.S. performed all of the mouse experiments and collection of samples for RNA-seq in the laboratory of T.J. R.H.H. performed all computational analyses of scRNA-seq data in the lab of A.R., with help from L.J.-A. A.B. performed bulk RNA-seq signature analysis. C.D. and M.H. provided technical assistance. C.G.R. supported TCR repertoire analyses in the laboratory of M.B. L.C., O.C.S., J.Y.K., and M.S.C. performed scRNA-seq in the laboratory of A.R., under guidance and supervision from O.R.-R. P.R. assisted with cell sorting. A.L., R.H.H., D.C., J.M.S., A.R., and T.J. wrote the manuscript with input from other authors.

DECLARATION OF INTERESTS

T.J. is a member of the Board of Directors of Amgen and Thermo Fisher Scientific. He is co-founder of Dragonfly Therapeutics and T2 Biosystems, and SAB member for Dragonfly Therapeutics, SQZ Biotech, and Skyhawk Therapeutics. None of these affiliations represent a conflict of interest with respect to the design or execution of this study or interpretation of data presented in this manuscript. T.J.'s laboratory also receives funding from the Johnson and Johnson Lung Cancer Initiative and Calico that did not support the research described in this manuscript. A.R. is a co-founder and equity holder in Celsius Therapeutics and an SAB member for Thermo Fisher, Neogene Therapeutics, and Syros Pharmaceuticals. A.L., R.H.H., A.R., and T.J. are co-inventors on a US provisional patent application (62/788,952) directed to overcoming immunosuppression.

Received: March 4, 2019
Revised: September 7, 2019
Accepted: October 29, 2019
Published: December 3, 2019

REFERENCES

Akama-Garren, E.H., Joshi, N.S., Tammela, T., Chang, G.P., Wagner, B.L., Lee, D.-Y., Rideout, W.M., 3rd, Papagiannakopoulos, T., Xue, W., and Jacks, T. (2016). A Modular Assembly Platform for Rapid Generation of DNA Constructs. Sci. Rep. *6*, 16836.

Ameri, A.H., Moradi Tuchayi, S., Zaalberg, A., Park, J.H., Ngo, K.H., Li, T., Lopez, E., Colonna, M., Lee, R.T., Mino-Kenudson, M., and Demehri, S. (2019). IL-33/regulatory T cell axis triggers the development of a tumor-promoting immune environment in chronic inflammation. Proc. Natl. Acad. Sci. USA *116*, 2646–2651.

Anderson, K.G., Sung, H., Skon, C.N., Lefrancois, L., Deisinger, A., Vezys, V., and Masopust, D. (2012). Cutting edge: intravascular staining redefines lung CD8 T cell responses. J. Immunol. *189*, 2702–2706.

Angerer, P., Haghverdi, L., Büttner, M., Theis, F.J., Marr, C., and Buettner, F. (2016). destiny: diffusion maps for large-scale single-cell data in R. Bioinformatics *32*, 1241–1243.

Arpaia, N., Green, J.A., Moltedo, B., Arvey, A., Hemmers, S., Yuan, S., Treuting, P.M., and Rudensky, A.Y. (2015). A Distinct Function of Regulatory T Cells in Tissue Protection. Cell *162*, 1078–1089.

Ashour, A.S., Samanta, S., Dey, N., Kausar, N., Abdessalemkaraa, W.B., and Hassanien, A.E. (2015). Computed tomography image enhancement using cuckoo search: a log transform based approach. J. Signal Inf. Process. *6*, 244.

Bankhead, P., Loughrey, M.B., Fernández, J.A., Dombrowski, Y., McArt, D.G., Dunne, P.D., McQuaid, S., Gray, R.T., Murray, L.J., Coleman, H.G., et al. (2017). QuPath: Open source software for digital pathology image analysis. Sci. Rep. *7*, 16878.

Bastian, M., Heymann, S., and Jacomy, M. (2009). In Gephi: an open source software for exploring and manipulating networks. International AAAI Conference on Weblogs and Social Media.

Bettelli, E., Carrier, Y., Gao, W., Korn, T., Strom, T.B., Oukka, M., Weiner, H.L., and Kuchroo, V.K. (2006). Reciprocal developmental pathways for the generation of pathogenic effector TH17 and regulatory T cells. Nature *441*, 235–238.

Biton, A., Bernard-Pierrot, I., Lou, Y., Krucker, C., Chapeaublanc, E., Rubio-Pérez, C., López-Bigas, N., Kamoun, A., Neuzillet, Y., Gestraud, P., et al. (2014). Independent component analysis uncovers the landscape of the bladder tumor transcriptome and reveals insights into luminal and basal subtypes. Cell Rep. *9*, 1235–1245.

Bos, P.D., Plitas, G., Rudra, D., Lee, S.Y., and Rudensky, A.Y. (2013). Transient regulatory T cell ablation deters oncogene-driven breast cancer and enhances radiotherapy. J. Exp. Med. *210*, 2435–2466.

Bullard, J.H., Purdom, E., Hansen, K.D., and Dudoit, S. (2010). Evaluation of statistical methods for normalization and differential expression in mRNA-Seq experiments. BMC Bioinformatics *11*, 94.

Burzyn, D., Kuswanto, W., Kolodin, D., Shadrach, J.L., Cerletti, M., Jang, Y., Sefik, E., Tan, T.G., Wagers, A.J., Benoist, C., and Mathis, D. (2013). A special population of regulatory T cells potentiates muscle repair. Cell *155*, 1282–1295.

Chen, W.-Y., Hong, J., Gannon, J., Kakkar, R., and Lee, R.T. (2015). Myocardial pressure overload induces systemic inflammation through endothelial cell IL-33. Proc. Natl. Acad. Sci. USA *112*, 7249–7254.

Cheng, G., Yuan, X., Tsai, M.S., Podack, E.R., Yu, A., and Malek, T.R. (2012). IL-2 receptor signaling is essential for the development of Klrg1+ terminally differentiated T regulatory cells. J. Immunol. *189*, 1780–1791.

De Simone, M., Arrigoni, A., Rossetti, G., Gruarin, P., Ranzani, V., Politano, C., Bonnal, R.J.P., Provasi, E., Sarnicola, M.L., Panzeri, I., et al. (2016). Transcriptional Landscape of Human Tissue Lymphocytes Unveils Uniqueness of Tumor-Infiltrating T Regulatory Cells. Immunity *45*, 1135–1147.

Delacher, M., Imbusch, C.D., Weichenhan, D., Breiling, A., Hotz-Wagenblatt, A., Träger, U., Hofer, A.-C., Kägebein, D., Wang, Q., Frauhammer, F., et al. (2017). Genome-wide DNA-methylation landscape defines specialization of regulatory T cells in tissues. Nat. Immunol. *18*, 1160–1172.

Dranoff, G. (2011). Experimental mouse tumour models: what can be learnt about human cancer immunology? Nat. Rev. Immunol. *12*, 61–66.

DuPage, M., Dooley, A.L., and Jacks, T. (2009). Conditional mouse lung cancer models using adenoviral or lentiviral delivery of Cre recombinase. Nat. Protoc. *4*, 1064–1072.

DuPage, M., Cheung, A.F., Mazumdar, C., Winslow, M.M., Bronson, R., Schmidt, L.M., Crowley, D., Chen, J., and Jacks, T. (2011). Endogenous T cell responses to antigens expressed in lung adenocarcinomas delay malignant tumor progression. Cancer Cell *19*, 72–85.

Fan, J., Salathia, N., Liu, R., Kaeser, G.E., Yung, Y.C., Herman, J.L., Kaper, F., Fan, J.-B., Zhang, K., Chun, J., and Kharchenko, P.V. (2016). Characterizing transcriptional heterogeneity through pathway and gene set overdispersion analysis. Nat. Methods *13*, 241–244.

Gibson, D.G., Young, L., Chuang, R.-Y., Venter, J.C., Hutchison, C.A., 3rd, and Smith, H.O. (2009). Enzymatic assembly of DNA molecules up to several hundred kilobases. Nat. Methods *6*, 343–345.

Green, J.A., Arpaia, N., Schizas, M., Dobrin, A., and Rudensky, A.Y. (2017). A nonimmune function of T cells in promoting lung tumor progression. J. Exp. Med. *214*, 3565–3575.

Guo, X., Zhang, Y., Zheng, L., Zheng, C., Song, J., Zhang, Q., Kang, B., Liu, Z., Jin, L., Xing, R., et al. (2018). Global characterization of T cells in non-small-cell lung cancer by single-cell sequencing. Nat. Med. *24*, 978–985.

Haghverdi, L., Buettner, F., and Theis, F.J. (2015). Diffusion maps for high-dimensional single-cell analysis of differentiation data. Bioinformatics *31*, 2989–2998.

Halim, L., Romano, M., McGregor, R., Correa, I., Pavlidis, P., Grageda, N., Hoong, S.-J., Yuksel, M., Jassem, W., Hannen, R.F., et al. (2017). An Atlas of Human Regulatory T Helper-like Cells Reveals Features of Th2-like Tregs that Support a Tumorigenic Environment. Cell Rep. *20*, 757–770.

Hall, A.O., Beiting, D.P., Tato, C., John, B., Oldenhove, G., Lombana, C.G., Pritchard, G.H., Silver, J.S., Bouladoux, N., Stumhofer, J.S., et al. (2012). The cytokines interleukin 27 and interferon-γ promote distinct Treg cell populations required to limit infection-induced pathology. Immunity *37*, 511–523.

Hyvärinen, A., and Oja, E. (2000). Independent component analysis: algorithms and applications. Neural Netw. *13*, 411–430.

Jackson, E.L., Olive, K.P., Tuveson, D.A., Bronson, R., Crowley, D., Brown, M., and Jacks, T. (2005). The differential effects of mutant p53 alleles on advanced murine lung cancer. Cancer Res. *65*, 10280–10288.

Jerby-Arnon, L., Shah, P., Cuoco, M.S., Rodman, C., Su, M.-J., Melms, J.C., Leeson, R., Kanodia, A., Mei, S., Lin, J.-R., et al. (2018). A Cancer Cell Program Promotes T Cell Exclusion and Resistance to Checkpoint Blockade. Cell *175*, 984–997.e24.

Johdi, N.A., Ait-Tahar, K., Sagap, I., and Jamal, R. (2017). Molecular Signatures of Human Regulatory T Cells in Colorectal Cancer and Polyps. Front. Immunol. *8*, 620.

Josefowicz, S.Z., Lu, L.-F., and Rudensky, A.Y. (2012). Regulatory T cells: mechanisms of differentiation and function. Annu. Rev. Immunol. *30*, 531–564.

Joshi, N.S., Akama-Garren, E.H., Lu, Y., Lee, D.-Y., Chang, G.P., Li, A., DuPage, M., Tammela, T., Kerper, N.R., Farago, A.F., et al. (2015). Regulatory T Cells in Tumor-Associated Tertiary Lymphoid Structures Suppress Anti-tumor T Cell Responses. Immunity *43*, 579–590.

Kim, B.-S., Lu, H., Ichiyama, K., Chen, X., Zhang, Y.-B., Mistry, N.A., Tanaka, K., Lee, Y.-H., Nurieva, R., Zhang, L., et al. (2017). Generation of RORγt$^+$ Antigen-Specific T Regulatory 17 Cells from Foxp3$^+$ Precursors in Autoimmunity. Cell Rep. *21*, 195–207.

Koch, M.A., Tucker-Heard, G., Perdue, N.R., Killebrew, J.R., Urdahl, K.B., and Campbell, D.J. (2009). The transcription factor T-bet controls regulatory T cell homeostasis and function during type 1 inflammation. Nat. Immunol. *10*, 595–602.

Koch, M.A., Thomas, K.R., Perdue, N.R., Smigiel, K.S., Srivastava, S., and Campbell, D.J. (2012). T-bet(+) Treg cells undergo abortive Th1 cell differentiation due to impaired expression of IL-12 receptor β2. Immunity *37*, 501–510.

Kolodin, D., van Panhuys, N., Li, C., Magnuson, A.M., Cipolletta, D., Miller, C.M., Wagers, A., Germain, R.N., Benoist, C., and Mathis, D. (2015). Antigen- and cytokine-driven accumulation of regulatory T cells in visceral adipose tissue of lean mice. Cell Metab. *21*, 543–557.

Langmead, B., Trapnell, C., Pop, M., and Salzberg, S.L. (2009). Ultrafast and memory-efficient alignment of short DNA sequences to the human genome. Genome Biol. *10*, R25.

Lee, C.-L., Moding, E.J., Huang, X., Li, Y., Woodlief, L.Z., Rodrigues, R.C., Ma, Y., and Kirsch, D.G. (2012). Generation of primary tumors with Flp recombinase in FRT-flanked p53 mice. Dis. Model. Mech. *5*, 397–402.

Li, B., and Dewey, C.N. (2011). RSEM: accurate transcript quantification from RNA-Seq data with or without a reference genome. BMC Bioinformatics *12*, 323.

Li, L., Zeng, Q., Bhutkar, A., Galván, J.A., Karamitopoulou, E., Noordermeer, D., Peng, M.-W., Piersigilli, A., Perren, A., Zlobec, I., et al. (2018). GKAP Acts as a Genetic Modulator of NMDAR Signaling to Govern Invasive Tumor Growth. Cancer Cell *33*, 736–751.e5.

Magnuson, A.M., Kiner, E., Ergun, A., Park, J.S., Asinovski, N., Ortiz-Lopez, A., Kilcoyne, A., Paoluzzi-Tomada, E., Weissleder, R., Mathis, D., et al. (2018). Identification and validation of a tumor-infiltrating Treg transcriptional signature conserved across species and tumor types. Proc. Natl. Acad. Sci. USA *115*, E10672–E10681.

Makkouk, A., and Weiner, G.J. (2015). Cancer immunotherapy and breaking immune tolerance: new approaches to an old challenge. Cancer Res. *75*, 5–10.

Marabelle, A., Kohrt, H., Sagiv-Barfi, I., Ajami, B., Axtell, R.C., Zhou, G., Rajapaksa, R., Green, M.R., Torchia, J., Brody, J., et al. (2013). Depleting tumor-specific Tregs at a single site eradicates disseminated tumors. J. Clin. Invest. *123*, 2447–2463.

Merico, D., Isserlin, R., Stueker, O., Emili, A., and Bader, G.D. (2010). Enrichment map: a network-based method for gene-set enrichment visualization and interpretation. PLoS One *11*, e13984.

Miettinen, J., Nordhausen, K., and Taskinen, S. (2017). Blind Source Separation Based on Joint Diagonalization in R: The Packages JADE and BSSasymp. Journal of Statistical Software *76*.

Miragaia, R.J., Gomes, T., Chomka, A., Jardine, L., Riedel, A., Hegazy, A.N., Whibley, N., Tucci, A., Chen, X., Lindeman, I., et al. (2019). Single-Cell Transcriptomics of Regulatory T Cells Reveals Trajectories of Tissue Adaptation. Immunity *50*, 493–504.e7.

Montoro, D.T., Haber, A.L., Biton, M., Vinarsky, V., Lin, B., Birket, S.E., Yuan, F., Chen, S., Leung, H.M., Villoria, J., et al. (2018). A revised airway epithelial hierarchy includes CFTR-expressing ionocytes. Nature *560*, 319–324.

Overacre-Delgoffe, A.E., Chikina, M., Dadey, R.E., Yano, H., Brunazzi, E.A., Shayan, G., Horne, W., Moskovitz, J.M., Kolls, J.K., Sander, C., et al. (2017). Interferon-γ Drives T_{reg} Fragility to Promote Anti-tumor Immunity. Cell *169*, 1130–1141.e11.

Panduro, M., Benoist, C., and Mathis, D. (2016). Tissue Tregs. Annu. Rev. Immunol. *34*, 609–633.

Pastille, E., Wasmer, M.-H., Adamczyk, A., Vu, V.P., Mager, L.F., Phuong, N.N.T., Palmieri, V., Simillion, C., Hansen, W., Kasper, S., et al. (2019). The IL-33/ST2 pathway shapes the regulatory T cell phenotype to promote intestinal cancer. Mucosal Immunol. *12*, 990–1003.

Picelli, S., Björklund, Å.K., Faridani, O.R., Sagasser, S., Winberg, G., and Sandberg, R. (2013). Smart-seq2 for sensitive full-length transcriptome profiling in single cells. Nat. Methods *10*, 1096–1098.

Plitas, G., Konopacki, C., Wu, K., Bos, P.D., Morrow, M., Putintseva, E.V., Chudakov, D.M., and Rudensky, A.Y. (2016). Regulatory T Cells Exhibit Distinct Features in Human Breast Cancer. Immunity *45*, 1122–1134.

Rau, A., Gallopin, M., Celeux, G., and Jaffrézic, F. (2013). Data-based filtering for replicated high-throughput transcriptome sequencing experiments. Bioinformatics *29*, 2146–2152.

Redjimi, N., Raffin, C., Raimbaud, I., Pignon, P., Matsuzaki, J., Odunsi, K., Valmori, D., and Ayyoub, M. (2012). CXCR3+ T regulatory cells selectively

accumulate in human ovarian carcinomas to limit type I immunity. Cancer Res. *72*, 4351–4360.

Rubtsov, Y.P., Rasmussen, J.P., Chi, E.Y., Fontenot, J., Castelli, L., Ye, X., Treuting, P., Siewe, L., Roers, A., Henderson, W.R., Jr., et al. (2008). Regulatory T cell-derived interleukin-10 limits inflammation at environmental interfaces. Immunity *28*, 546–558.

Rutledge, D.N., and Jouan-Rimbaud Bouveresse, D. (2013). Independent Components Analysis with the JADE algorithm. Trends Analyt. Chem. *50*, 22–32.

Saito, T., Nishikawa, H., Wada, H., Nagano, Y., Sugiyama, D., Atarashi, K., Maeda, Y., Hamaguchi, M., Ohkura, N., Sato, E., et al. (2016). Two FOXP3(+) CD4(+) T cell subpopulations distinctly control the prognosis of colorectal cancers. Nat. Med. *22*, 679–684.

Sánchez-Rivera, F.J., Papagiannakopoulos, T., Romero, R., Tammela, T., Bauer, M.R., Bhutkar, A., Joshi, N.S., Subbaraj, L., Bronson, R.T., Xue, W., and Jacks, T. (2014). Rapid modelling of cooperating genetic events in cancer through somatic genome editing. Nature *516*, 428–431.

Sha, Y., Phan, J.H., and Wang, M.D. (2015). Effect of low-expression gene filtering on detection of differentially expressed genes in RNA-seq data. Conf. Proc. IEEE Eng. Med. Biol. Soc. *2015*, 6461–6464.

Shalek, A.K., Satija, R., Adiconis, X., Gertner, R.S., Gaublomme, J.T., Raychowdhury, R., Schwartz, S., Yosef, N., Malboeuf, C., Lu, D., et al. (2013). Single-cell transcriptomics reveals bimodality in expression and splicing in immune cells. Nature *498*, 236–240.

Shang, B., Liu, Y., Jiang, S.-J., and Liu, Y. (2015). Prognostic value of tumor-infiltrating FoxP3^{+} regulatory T cells in cancers: a systematic review and meta-analysis. Sci. Rep. *5*, 15179.

Simpson, T.R., Li, F., Montalvo-Ortiz, W., Sepulveda, M.A., Bergerhoff, K., Arce, F., Roddie, C., Henry, J.Y., Yagita, H., Wolchok, J.D., et al. (2013). Fc-dependent depletion of tumor-infiltrating regulatory T cells co-defines the efficacy of anti-CTLA-4 therapy against melanoma. J. Exp. Med. *210*, 1695–1710.

Singer, M., Wang, C., Cong, L., Marjanovic, N.D., Kowalczyk, M.S., Zhang, H., Nyman, J., Sakuishi, K., Kurtulus, S., Gennert, D., et al. (2017). A Distinct Gene Module for Dysfunction Uncoupled from Activation in Tumor-Infiltrating T Cells. Cell *171*, 1221–1223.

Singh, P., and Shree, R. (2016). Analysis and effects of speckle noise in SAR images. In Proceedings of the 2016 2nd International Conference on Advances in Computing, Communication, Automation (ICACCA), pp. 1–5.

Soria, J.-C., Marabelle, A., Brahmer, J.R., and Gettinger, S. (2015). Immune checkpoint modulation for non-small cell lung cancer. Clin. Cancer Res. *21*, 2256–2262.

Stubbington, M.J.T., Lönnberg, T., Proserpio, V., Clare, S., Speak, A.O., Dougan, G., and Teichmann, S.A. (2016). T cell fate and clonality inference from single-cell transcriptomes. Nat. Methods *13*, 329–332.

Subramanian, A., Tamayo, P., Mootha, V.K., Mukherjee, S., Ebert, B.L., Gillette, M.A., Paulovich, A., Pomeroy, S.L., Golub, T.R., Lander, E.S., and Mesirov, J.P. (2005). Gene set enrichment analysis: a knowledge-based approach for interpreting genome-wide expression profiles. Proc. Natl. Acad. Sci. USA *102*, 15545–15550.

Suzuki, K., Kadota, K., Sima, C.S., Nitadori, J., Rusch, V.W., Travis, W.D., Sadelain, M., and Adusumilli, P.S. (2013). Clinical impact of immune microenvironment in stage I lung adenocarcinoma: tumor interleukin-12 receptor β2 (IL-12Rβ2), IL-7R, and stromal FoxP3/CD3 ratio are independent predictors of recurrence. J. Clin. Oncol. *31*, 490–498.

Tan, T.G., Mathis, D., and Benoist, C. (2016). Singular role for T-BET+CXCR3+ regulatory T cells in protection from autoimmune diabetes. Proc. Natl. Acad. Sci. USA *113*, 14103–14108.

Tanaka, A., and Sakaguchi, S. (2017). Regulatory T cells in cancer immunotherapy. Cell Res. *27*, 109–118.

Treutlein, B., Brownfield, D.G., Wu, A.R., Neff, N.F., Mantalas, G.L., Espinoza, F.H., Desai, T.J., Krasnow, M.A., and Quake, S.R. (2014). Reconstructing lineage hierarchies of the distal lung epithelium using single-cell RNA-seq. Nature *509*, 371–375.

Vasanthakumar, A., Moro, K., Xin, A., Liao, Y., Gloury, R., Kawamoto, S., Fagarasan, S., Mielke, L.A., Afshar-Sterle, S., Masters, S.L., et al. (2015). The transcriptional regulators IRF4, BATF and IL-33 orchestrate development and maintenance of adipose tissue-resident regulatory T cells. Nat. Immunol. *16*, 276–285.

Wan, Y.Y., and Flavell, R.A. (2005). Identifying Foxp3-expressing suppressor T cells with a bicistronic reporter. Proc. Natl. Acad. Sci. USA *102*, 5126–5131.

Young, N.P., Crowley, D., and Jacks, T. (2011). Uncoupling cancer mutations reveals critical timing of p53 loss in sarcomagenesis. Cancer Res. *71*, 4040–4047.

Zhang, L., Yu, X., Zheng, L., Zhang, Y., Li, Y., Fang, Q., Gao, R., Kang, B., Zhang, Q., Huang, J.Y., et al. (2018). Lineage tracking reveals dynamic relationships of T cells in colorectal cancer. Nature *564*, 268–272.

Zheng, C., Zheng, L., Yoo, J.-K., Guo, H., Zhang, Y., Guo, X., Kang, B., Hu, R., Huang, J.Y., Zhang, Q., et al. (2017). Landscape of Infiltrating T Cells in Liver Cancer Revealed by Single-Cell Sequencing. Cell *169*, 1342–1356.e16.

STAR★METHODS

KEY RESOURCES TABLE

REAGENT or RESOURCE	SOURCE	IDENTIFIER
Antibodies		
KLRG1 2F1 PE-Cy7	Thermo Fisher	RRID: AB_1518768
CD103 2E7 APC	BioLegend	RRID: AB_1227502
CD4 RM4-5 APC-eFluor780	Thermo Fisher	RRID: AB_1272183
Foxp3 FJK-16 s FITC	Thermo Fisher	RRID: AB_465243
IL-17 eBio17B7 PerCP-Cy5.5	Thermo Fisher	RRID: AB_925753
CD44 IM7 Alexa Fluor 700	Thermo Fisher	RRID: AB_494011
CD62L MEL-14 eFluor450	Thermo Fisher	RRID: AB_1963590
CCR6 29-2L17 PE/Dazzle 594	BioLegend	RRID: AB_2687019
RORgt Q31-378 Alexa Fluor 647	BD Biosciences	RRID: AB_2738916
T-bet O4-46 PE	BD Biosciences	RRID: AB_10564071
PD-1 J43 PE-Cy7	BioLegend	RRID: AB_572017
CD69 H1.2F3 BV785	BioLegend	RRID: AB_2629640
CXCR3 CXCR3-173 BV421	BD Biosciences	RRID: AB_10900974
ST2 U29-93 Brilliant Blue 700	BD Biosciences	RRID: AB_2743483
CD85k H1.1 PE	Biolegend	RRID: AB_2561653
Ki-67 B56 BV786	BD Biosciences	RRID: AB_2732007
CD45.2 104 V500	BD Biosciences	RRID: AB_10897142
Thy1.2 30-H12 APC-eFluor780	Thermo Fisher	RRID: AB_1272187
CD103 2E7 BV510	BioLegend	RRID: AB_2562713
CD4 RM4-5 BUV737	BD Biosciences	RRID: AB_2738734
CD8a 53-6.7 BUV395	BD Biosciences	RRID: AB_2739421
CD45 30-F11 PE-CF594	BD Biosciences	RRID: AB_11154401
CD45 30-F11 APC-Ef780	Thermo Fisher	RRID: AB_1548781
CXCR6 SA051D1 PE/Dazzle 594	Biolegend	RRID: AB_2721700
KLRG1 2F1 BV711	BioLegend	RRID: AB_2629721
CD11c HL3 PE-Cy7	BD Biosciences	RRID: AB_469590
Siglec F E50-2440 PE	BD Biosciences	RRID: AB_394341
CD4 RM4-4 PE	Biolegend	RRID: AB_313691
CD8b eBioH35-17.2 PE	Thermo Fisher	RRID: AB_657768
IHC and IF: Goat anti-mouse IL-33	R&D Biosystems	RRID: AB_884269
IHC: Rat anti-mouse CD8alpha	Thermo Fisher	RRID: AB_2637159
IF: Rabbit anti-mouse proSP-C	Millipore	RRID: AB_91588
Chemicals, Peptides, and Recombinant Proteins		
Recombinant mouse IL-33	BioLegend	Biolegend 580506
Cell Stimulation Cocktail	Thermo Fisher	Cat: 00-4970-03
SIINFEKL-Kb monomer	NIH Tetramer Core	
Critical Commercial Assays		
Thru-Plex-FD Library Prep Kit	Rubicon Genomics	
Nextera XT Library Prep Kit	Illumina	FC-131-1096
Deposited Data		
Bulk and single cell RNA sequencing	GEO	GEO: GSE139232

(*Continued on next page*)

Continued

REAGENT or RESOURCE	SOURCE	IDENTIFIER
Experimental Models: Organisms/Strains		
Mouse: B6.129S4-Krastm4Tyj/J		RRID: IMSR_JAX:008179
Mouse: B6.129P2-Trp53tm1Brn/J	Jackson Laboratory	RRID: IMSR_JAX:008462
Mouse: C57BL/6-Foxp3tm1Flv/J		RRID: IMSR_JAX:008374
Mouse: Foxp3tm1Kuch	Bettelli et al., 2006	MGI:3718527
Mouse: B6.129(Cg)-Foxp3tm4(YFP/icre)Ayr/J	Jackson Laboratory	RRID: IMSR_JAX:016959
Mouse: Il1rl1tm1.1Rlee	Chen et al., 2015	MGI:5818148
Oligonucleotides		
See Table S7.	This paper	N/A
Recombinant DNA		
Plasmid: Lenti-LucOS	Addgene	Addgene_22777
Plasmid: pGK::GFP-LucOS::EFS::FlpO (FlpO-GFP-OS)	This paper	Available upon request
Software and Algorithms		
Code generated for this study	This paper	Available upon request
SCDE	Fan et al., 2016	http://hms-dbmi.github.io/scde/
Bowtie	Langmead et al., 2009	http://bowtie-bio.sourceforge.net/bowtie2/index.shtml
RSEM v1.2.8	Li and Dewey, 2011	https://bmcbioinformatics.biomedcentral.com/articles/10.1186/1471-2105-12-323
JADE v1.1.0	Miettinen et al. 2017	https://cran.r-project.org/web/packages/JADE/index.html
Tracer	Stubbington et al., 2016	https://github.com/Teichlab/tracer
Gephi	Bastian et al., 2009	https://gephi.org
EnrichmentMap (Cytoscape)	Merico et al., 2010	https://www.cytoscape.org
QuPath	Bankhead et al., 2017	https://qupath.github.io/
Prism	GraphPad	

LEAD CONTACT AND MATERIALS AVAILABILITY

Further information and requests for resources and reagents should be directed to and will be fulfilled by the Lead Contact Tyler Jacks (tjacks@mit.edu). Plasmids generated in this study are being submitted to Addgene. All unique/stable reagents generated in this study are available from the Lead Contact upon request.

EXPERIMENTAL MODEL AND SUBJECT DETAILS

Mice

KP, KPfrt, *Foxp3*^{GFP}, *Foxp3*^{RFP}, *Foxp3*$^{YFP/Cre}$, and *Il1rl1*$^{fl/fl}$ mice, all on a C57BL/6 background, have been previously described (Bettelli et al., 2006; Chen et al., 2015; DuPage et al., 2011; Rubtsov et al., 2008; Wan and Flavell, 2005; Young et al., 2011). Both male and female mice were used for all experiments, and mice were gender and age-matched within experiments. Experimental and control mice were co-housed whenever appropriate. All studies were performed under an animal protocol approved by the Massachusetts Institute of Technology (MIT) Committee on Animal Care. Mice were assessed for morbidity according to MIT Division of Comparative Medicine guidelines and humanely sacrificed prior to natural expiration.

METHOD DETAILS

Mouse studies

For *in vivo* labeling of circulating immune cells, anti-CD4-PE (eBioscience, RM4-4, 1:400) and anti-CD8β-PE (eBioscience, 1:400) were diluted in PBS and administered by IV injection 5 minutes before harvest (Anderson et al., 2012). Alternatively, anti-CD45-PE-CF594 (30-F11, BD Biosciences, 1:200) was also used for intravascular labeling and was administered 2 minutes before sacrifice.

Lentiviral production and tumor induction

The lentiviral backbone Lenti-LucOS has been described previously (DuPage et al., 2011). Lentiviral plasmids and packaging vectors were prepared using endo-free maxiprep kits (QIAGEN). The pGK::GFP-LucOS::EFS::FlpO lentiviral plasmid was cloned using Gibson assembly (Akama-Garren et al., 2016; Gibson et al., 2009). Briefly, GFP-OS was created as a protein fusion of GFP and ovalbumin$_{257-383}$, which includes the SIINFEKL and AAHAEINEA epitopes, and SIYRYYGL antigen. Lentiviral plasmids and packaging vectors were prepared using endo-free maxiprep kits (QIAGEN). Lentiviruses were produced by co-transfection of 293FS* cells with Lenti-LucOS or FlpO-GFP-OS, psPAX2 (gag/pol), and VSV-G vectors at a 4:3:1 ratio, respectively, with Mirus TransIT LT1 (Mirus Bio, LLC). Virus-containing supernatant was collected 48 and 72h after transfection and filtered through 0.45mm filters before concentration by ultracentrifugation (25,000 RPM for 2 hours with low decel). Virus was then resuspended in 1:1 Opti-MEM (GIBCO) - HBSS. Aliquots of virus were stored at −80°C and titered using the GreenGo 3TZ cell line (Sánchez-Rivera et al., 2014).

For tumor induction, mice between 8-15 weeks of age received 2.5 x10^4 PFU of Lenti-LucOS or 4.5 × 10^4 PFU of FlpO-GFP-OS intratracheally as described previously (DuPage et al., 2009).

Tissue isolation and preparation of single cell suspensions

After sacrifice, lungs were placed in 2.5mL collagenase/DNase buffer (Joshi et al., 2015) in gentleMACS C tubes (Miltenyi) and processed using program m_impTumor_01.01. Lungs were then incubated at 37°C for 30 minutes with gentle agitation. The tissue suspension was filtered through a 100 μm cell strainer and centrifuged at 1700 RPM for 10 minutes. Red blood cell lysis was performed by incubation with ACK Lysis Buffer (Life Technologies) for 3 minutes. Samples were filtered and centrifuged again, followed by resuspension in RPMI 1640 (VWR) supplemented with 1% heat-inactivated FBS and 1X penicillin-streptomycin (GIBCO), and 1X L-glutamine (GIBCO).

Spleens and lymph nodes were dissociated using the frosted ends of microscope slides into RPMI 1640 supplemented with 1% heat-inactivated FBS and 1X penicillin-streptomycin (GIBCO), and 1X L-glutamine (GIBCO). Spleen cell suspensions were spun down at 1500 RPM for 5 minutes, and red blood cell lysis with ACK Lysis Buffer was performed for 5 minutes. Cells were filtered through 40 μm nylon mesh and, after centrifugation, resuspended in supplemented RPMI 1640. Lymph node suspensions were filtered through a 40 μm nylon mesh, spun down at 1500 RPM for 5 minutes, and resuspended in supplemented RPMI 1640.

For *ex vivo* T cell stimulation experiments to detect intracellular cytokines, 0.5 × 10^5 cells were plated in a 96-well U-bottom plate (BD Biosciences) in RPMI 1640 (VWR) supplemented with 10% heat-inactivated FBS, 1X penicillin-streptomycin (GIBCO), 1X L-glutamine (GIBCO), 1X HEPES (GIBCO), 1X GlutaMAX (GIBCO), 1mM sodium pyruvate (Thermo Fisher), 1X MEM non-essential amino acids (Sigma), 50μM β-mercaptoethanol (GIBCO), 1X Cell Stimulation Cocktail (eBioscience), 1X monensin (BioLegend), and 1X brefeldin A (BioLegend). Cells were incubated in a tissue culture incubator at 37°C with 5% CO_2 for 4 hours.

Staining for flow cytometric analysis

Approximately 0.5-1 × 10^6 cells were stained for 15-30 minutes at 4°C in 96-well U-bottom plates (BD Biosciences) with directly conjugated antibodies (Table S7). SIINFEKL-Kb tetramer was prepared using streptavidin-APC (Prozyme) and SIINFEKL-Kb monomer from the NIH Tetramer Core.

After staining, cells were fixed with Cytofix/ Cytoperm Buffer (BD). Samples that were destined for Foxp3 or other transcription factor staining were fixed with the Foxp3 Transcription Factor Staining Buffer Kit (eBioscience). Intracellular cytokine and transcription factor staining were performed right before analysis using either the BD Perm/Wash Buffer (BD) or the Foxp3 Transcription Factor Staining Buffer Kit (eBioscience); staining was performed for 45 minutes at 4°C. Analysis of T_{regs} (i.v.^{neg}CD4$^+$Foxp3$^+$) and T_{conv} (i.v.^{neg}CD4$^+$Foxp3$^-$) was performed on an LSR II (BD) with 405, 488, 561, and 635 lasers. Data analysis was performed using FlowJo software.

Isolation of T_{reg} populations for bulk RNA-Seq

For sequencing of CD103$^-$KLRG1$^-$ (DN), CD103$^+$KLRG1$^-$ (SP), and CD103$^+$KLRG1$^+$ (DP) T_{regs}: 100-200 DP, SP, and DN T_{reg} cells from LucOS-infected, KP, *Foxp3^{RFP}* mice were sorted using a MoFlo Astrios cell sorter. cDNA was prepared by the SMART-Seq2 protocol (Picelli et al., 2013) with the following modifications: RNA was purified using 2.2X RNAclean SPRI beads (Beckman Coulter) without final elution, after which beads were air-dried and immediately resuspended with water and oligoDT for annealing, and 18 cycles of preamplification were used for cDNA. cDNA was then mechanically sheared and prepared into sequencing libraries using the Thru-Plex-FD Kit (Rubicon Genomics). Sequencing was performed on an Illumina HiSeq 2000 instrument to obtain 50 nt paired-end reads.

For comparison of KPF and KPF-ST2^{FL} T_{regs}: 100-200 DP, SP, and DN T_{regs} were sorted into Buffer TCL (QIAGEN) plus 1% β-mercaptoethanol and cDNA was prepared with 14 cycles of preamplification. Nextera library preparation was performed as previously described (Picelli et al., 2013) and sequencing was performed with 50 × 25 paired end reads using two kits on the NextSeq500 5 instrument.

Single-cell sorting of T_{conv} and T_{reg} populations for RNA sequencing

T_{conv} (DAPI^{neg}, i.v.^{neg}, Thy1.2^{+}CD4^{+}Foxp3^{-}GFP^{neg}) and T_{reg} (DAPI^{neg}, i.v.^{neg}, Thy1.2^{+}CD4^{+}Foxp3^{-}GFP^{pos}) cells were isolated from ~4 mice per time point and single-cell sorted into Buffer TCL (QIAGEN) plus 1% β-mercaptoethanol in 96-well plates using a MoFlo Astrios cell sorter. Each plate had a 30-100 cell population well and an empty well as controls. Following sorting, plates were spun down for 1" at 2000 RPM and frozen immediately at −80C.

Droplet-based scRNA-seq of CD45^{+} and CD45^{-} populations from tumor-bearing lungs

Tumors were microdissected under dissection microscope and dissociated into single cell suspensions as previously described. Samples were pelleted at 1700 RPM for 5 minutes and resuspended in 500ul of MACS buffer containing PBS, 0.5% bovine serum albumin (BSA), and 2mM EDTA. CD45^{+} and CD45^{-} cells were then magnetically separated using MACS CD45 MicroBeads (Miltenyi Biotec) as per manufacturer's instructions. Briefly, cells were stained with CD45 MicroBeads for 15 minutes at 4°C. Samples were washed with MACS buffer and pelleted at 1700rpm for 5 minutes. Samples were resuspended in 1ml of MACS buffer and added to LS MACS column on LS Separator magnet (Miltenyi Biotec). Flow through was collected as CD45^{-} population. Columns were washed 3x with MACS buffer and flow-through was added to CD45^{-} population. 5ml of MACS buffer was then then added to column, the column was removed from the magnet, and cells were expelled from column into conical using plunger; this was the CD45^{+} sample. CD45^{+} and CD45^{-} samples were pelleted at 1700RPM for 5 minutes and resuspended in PBS with 0.01% BSA before proceeding to droplet based scRNaseq.

Single cells were processed through the 10X Genomics Single Cell 3′ platform using the Chromium Single Cell 3′ Library & Gel Bead Kit V2 kit (10X Genomics), per manufacturer's protocol. Briefly, 6,000 cells were loaded onto each channel and partitioned into Gel Beads in Emulsion in the Chromium instrument. Cell lysis and barcoding occur, followed by amplification, fragmentation, adaptor ligation and index library PCR. Libraries were sequenced on an Illumina HiSeqX at a read length of 98 base pairs.

Preparation of scRNaseq libraries

Plates were thawed and RNA was purified using 2.2X RNAclean SPRI beads (Beckman Coulter) without final elution (Shalek et al., 2013). SMART-seq2 and Nextera library preparation was performed as previously described (Picelli et al., 2013), with some modifications as described in a previous study (Singer et al., 2017). Plates were pooled into 384 single-cell libraries, and sequenced 50 × 25 paired end reads using a single kit on the NextSeq500 5 instrument.

Quantitative PCR for validation of RNA-Seq experiments

Quantitative PCR was performed using various primer sets (Table S7). 1ng of cDNA generated using SMART-Seq2 was included in a reaction with 1μL of each primer (2μM stock) and 5μL of KAPA SYBR Fast LightCycler 480 (KAPA Biosystems). Cp values were measured using a LightCycler 480 Real-Time PCR System (Roche). Relative fold-change in expression values were calculated using the following formula: $2^{(\Delta Cp(Sample) - \Delta Cp(Spleen))}$, where ΔCp(Sample) = Sample $Cp_{Gene\ of\ Interest}$ - Sample Cp_{GAPDH}, and ΔCp(Spleen) = Spleen $Cp_{Gene\ of\ Interest}$ - Spleen Cp_{GAPDH}.

Immunohistochemistry (IHC) and immunofluorescence staining

Lung lobes and spleens allocated for IHC and IF were perfused with 4% paraformaldehyde in PBS and fixed overnight at 4°C. Lung lobes and/ or spleen were transferred to histology cassettes and stored in 70% ethanol until paraffin embedding and sectioning (KI Histology Facility). H&E stains were performed by the core facility using standard methods.

For IHC, 5 μm unstained slides were dewaxed, boiled in citrate buffer (1 g NaOH, 2.1 g citric acid in 1L H2O, pH 6), for 5 minutes at 125°C in a decloaking chamber (Biocare Medical), washed with 3X with 0.1% Tween-20 (Sigma) in TBS, and blocked and stained in Sequenza slide racks (Thermo Fisher). Slides were blocked with Dual Endogenous Peroxidase and Alkaline Phosphatase Block (Dako) and then with 2.5% Horse Serum (Vector Labs). Slides were incubated in primary antibody overnight, following by washing and incubation in HRP-polymer-conjugated secondary antibodies (ImmPRESS HRP mouse-adsorbed anti-rat and anti-goat, Vector Laboratories). Slides were developed with ImmPACT DAB (Vector Laboratories). Primary antibodies used were goat anti-IL-33 (R&D, AF3626), rat anti-CD8a (Thermo Fisher, 4SM16), and rat anti-Foxp3 (Thermo Fisher, FJK-16 s). Stains were counterstained with hematoxylin using standard methods before dehydrating and mounting.

After fixation, lung lobes and spleen allocated for IF were perfused with 30% sucrose in PBS for cryoprotection for 6-8h at 4°C. Tissues were then perfused with 30% optimum cutting temperature (O.C.T.) compound (Tissue-Tek) in PBS and frozen in 100% O.C.T in cryomolds on dry ice. 6μm sections were cut using a CryoStar NX70 cryostat (Thermo), and air-dried for 60-90 minutes at room temperature. Sections were incubated in ice-cold acetone (Sigma) for 10 minutes at −20°C and then washed 3 × 5 minutes with PBS. Samples were permeabilized with 0.1% Triton X-100 (Sigma) in PBS followed by blocking with 0.5% PNB in PBS (Perkin Elmer). Primary antibodies were incubated overnight. Primary antibodies used were rabbit anti-prosurfactant protein C (SPC) (Millipore, AB3786, 1:500) and goat anti-IL-33 (R&D, AF3626, 1:200). After washing 3 × 5 minutes, samples were incubated in species-specific secondary antibodies conjugated to Alexa Fluor 568 and Alexa Fluor 488, respectively, at 1:500. Sections were then fixed in 1% PFA and mounted using Vectashield mounting media with DAPI (Vector Laboratories).

Immunohistochemistry and immunofluorescence tissue section images were acquired using a Nikon 80 Eclipse 80i fluorescence microscope using 10x and 20x objectives and an attached Andor camera. Stained IHC slides were scanned using the Aperio ScanScope AT2 at 20X magnification.

QUANTIFICATION AND STATISTICAL ANALYSIS

Bulk RNA-seq data pre-processing

Bulk RNA-Seq reads that passed quality metrics were mapped to the annotated UCSC mm9 mouse genome build (http://genome.ucsc.edu/) using RSEM (v1.2.12) (http://deweylab.github.io/RSEM/) (Li and Dewey, 2011) using RSEM's default Bowtie (v1.0.1) alignment program (Langmead et al., 2009). Expected read counts estimated from RSEM were upper-quartile normalized to a count of 1000 per sample (Bullard et al., 2010). Genes with normalized counts less than an upper-quartile threshold of 20 across all samples were considered lowly expressed and excluded from further analyses to increase the robustness of signature scoring, as previously described (Rau et al., 2013; Sha et al., 2015). As outlined below, signature analyses were conducted either on a $\log_2$ transformed version of the filtered gene expression matrix to overcome data skewness, or on the non-transformed version for increased sensitivity by avoiding compression of weaker signals (Ashour et al., 2015; Singh and Shree, 2016).

Signature analysis in bulk RNA-Seq

Signature analyses between bulk T_{reg} cell populations were performed using a blind source separation methodology based on Independent Component Analysis (ICA) (Hyvärinen and Oja, 2000), using the R implementation of the core JADE algorithm (Joint Approximate Diagonalization of Eigenmatrices) (Biton et al., 2014; Miettinen et al., 2017; Rutledge and Jouan-Rimbaud Bouveresse, 2013) along with custom R utilities. Multi-sample signatures were visualized using relative signature profile boxplots (Li et al., 2018). Heatmaps were generated with the Heatplus package in R using agglomerative hierarchical clustering with default euclidean distance measure, Ward's minimum variance method for row-clustering, and complete linkage for column clustering (Figures 4D and S2H).

DP T_{reg} signature

We identified a signature distinguishing $CD103^+KLRG1^+$ lung T_{regs} from other populations. The non-transformed expression matrix was decomposed using ICA with the JADE algorithm (described above) as: $\boldsymbol{E} = \boldsymbol{AS}$ where $\boldsymbol{E}$ is the expression matrix (input), $\boldsymbol{A}$ is the mixing matrix (mixing weights, basis vectors), and $\boldsymbol{S}$ is the signature matrix (independent components or latent variables yielding standardized gene-scores per signature). Biologically relevant signatures were identified through two approaches: (1) Quantitative assessment of significance using a 2-sample Mann-Whitney-Wilcoxon non-parametric test between mixing weights (from $\boldsymbol{A}$) grouped by biological condition per signature; and (b) visual inspection of a Hinton plot derived from the mixing matrix $\boldsymbol{A}$. Corresponding signatures from $\boldsymbol{S}$ were selected for downstream analyses. Up and down genes per signature were selected using a $|\text{gene-score}| >= 3$ threshold (standardized score, #s.d. above/below mean). Genes with $|\text{z-score}| > 3$ were selected for downstream analysis (75 upregulated and 31 downregulated genes). An additional expression level filter was implemented to narrow the list of genes of interest. For upregulated genes, expression in all $CD103^+KLRG1^+$ lung T_{reg} samples had to be greater than all but a maximum of 3 other samples (3 out of a total 8 other samples). A similar filtering scheme was employed in the other direction for downregulated genes. This yielded a total of 43 upregulated and 2 downregulated genes in $CD103^+KLRG1^+$ lung T_{regs}. This set of genes was used to illustrate gene expression level changes across samples (Figure S2H).

ST2-deficient T_{regs} Signature

A signature distinguishing ST2-deficient T_{regs} from wild-type T_{regs} (Table S5) was identified using ICA on the non-transformed expression matrix. To identify particular genes of interest, signature genes ($|\text{z-score}| > 3$) were filtered to include only genes that had an absolute fold change exceeding 1.5x within any of the $CD103^+KLRG1^+$ (DP), $CD103^+KLRG1^-$ (SP), $CD103^-KLRG1^-$ (DN) sample types between wild-type and ST2-deficient T_{regs}. These gene lists were further filtered to retain only those genes that appeared in at least two of the three sample types (i.e., up/downregulated in wild-type or ST2-deficient in at least two of DP/DN/SP comparisons). Genes with opposite directionality across the three sample types (n = 5 genes) were dropped. Expression levels of the resulting curated set of 14 genes were visualized using a row-normalized heatmap (Figure 4D). Signature correlation scores (z-scores) for each gene are included in Table S5.

Gene Set Enrichment Analysis (GSEA)

Selected signatures (from **S**) were run through the Gene Set Enrichment Analysis (GSEA) using the rank-based input format. All genes per signature were used, ranked by gene-scores from $\boldsymbol{S}$. We used gene-sets from MsigDB v5.1 (Subramanian et al., 2005). Custom gene set additions were made to version 4.0 of the MSigDB immunologic signatures library (c7) (Table S6). Normalized Enrichment Score (NES), p values and FDR for the custom gene-sets were calculated in the context of the combined c7 v4.0 MSigDB collection.

Network representations of GSEA results were generated using EnrichmentMap (http://www.baderlab.org/Software/EnrichmentMap) for Cytoscape v3.3.0 (https://www.cytoscape.org/).

Pre-processing of SMART-Seq2 scRNA-seq data

BAM files were converted to de-multiplexed FASTQs using the Illumina-provided *Bcl2Fastq* software package v2.17.1.14. Paired-end reads were mapped to the UCSC mm10 mouse transcriptome using Bowtie with parameters '-n 0 -m 10', which allows alignment of sequences with zero mismatches and allows for multi-mapping of a maximum of ten times.

Expression levels of genes were quantified using TPM values calculated by RSEM v1.2.8 in paired-end mode. For each cell, the number of detected genes (TPM > 0) was calculated and cells with less than 600 or more than 4,000 genes detected were excluded as well as cells that had a mapping rate to the transcriptome below 15%. To further remove potential doublets (mostly of B cells and epithelial cells), we calculated the sum $\log_2$(TPM+1) over *Cd79a*, *Cd19*, *Lyz1*, *Lyz2* and *Sftpc*, and excluded any cell that scored higher than 3. We retained only genes expressed above $\log_2$TPM of 3 in at least five cells in the whole dataset.

Since we could not sort for T_{reg} for two of the mice (#336 and #338), we had to infer which cells are T_{regs} from these data. To this end, we trained a random forest classifier for mice for which we have sorted both T_{conv} and T_{regs}, using the train function from the *caret* package in R, based on the expression of the following genes: *Foxp3*, *Ikzf2*, *Areg*, *Il1rl1*, *Folr4*, *Wls*, *Tnfrsf9*, *Klrg1*, *Il2ra*, *Dusp4*, *Ctla4*, *Neb*, *Itgb1*, and *Cd40lg*. The labeled data was partitioned into training and test sets. The model has a sensitivity and specificity above 90% in cross validation. We then applied the classifier on the unlabeled data and cells with a probability above 0.6 to be either T_{conv} or T_{reg} were given the corresponding label. The remaining 4% of cells were discarded as unambiguous.

Identifying tissue-specific gene programs for T_{reg} and T_{conv}

To identify genes that are differentially expressed between lung and msLN in T_{reg} and/or T_{conv}, we performed a regression analysis. We focused on the proportion of cells expressing a gene, and hence on logistic regression. We performed logistic regression using the bayesglm function from the *arm* package in R, including only those mice (# 338, #3642, #3839, #3889) for which we had matched cells from both lung and msLN, as well as for T_{reg} and T_{conv}, and excluding all genes expressed in > 95% or < 5% of cells in lung and msLN. We ran the logistic regression with expression data binarized at a $\log_2$(TPM+1) of 2 and using the following full model: *gene expression* ~*genes detected* + *batch effect* + *tissue* versus a reduced model: *gene expression* ~*genes detected* + *batch effect*. We corrected for multiple hypothesis by computing an FDR of the likelihood ratio test p value, and retained genes as differentially expressed between lung and msLN with $p < 10^{-5}$ and an |coefficient| > 2.

Comparing the extent of cell heterogeneity between lung and msLN

Diffusion components were calculated on a gene expression matrix limited to genes that were differentially expressed between lung and msLN using the DiffusionMap function from the *destiny* package in R (Angerer et al., 2016) with a *k* of 30 and a local sigma. In order to be able to compare the variance in distributions in diffusion component 1 and 2 between lung and msLN T_{reg}/T_{conv}, we downsampled the cells from the lung to the (lower) numbers of cells from the msLN. To test for significant differences in variance in the distributions of lung and msLN T_{reg}/T_{conv}, we used Levene's test for the equality of variances on the distributions of the coefficients of the downsampled cells in each of diffusion components 1 and 2.

Identifying gene programs and their time dependence

Gene programs were identified using PAGODA using the *scde* R package version 2.6.0. (Fan et al., 2016) on the counts table from RSEM after cleaning the data using the clean.counts function (min.lib.size = 600,min.detected = 5). The *knn.error.model* function was run using a *k* of 30, which is much lower than default, but yields statistically indistinguishable results from the default k (# cells / 4). We then ran the *pagoda.varnorm* to normalize gene expression variance, and the *pagoda.subtract.aspect* function to control for sequencing depth which then allowed us to run *pagoda.gene.clusters* which identifies *de-novo* correlated genes in the dataset. We forced PAGODA to return 100 programs. We identified programs with a significance z.score above 1.96. We removed several highly significant newly identified gene programs consisting of paralog groups with high expression correlation, likely because of multimapping of reads.

Mean program expression was calculated by averaging over the genes in each program of the centered and scaled gene expression table and transforming to a z-score over 1,000 randomly selected gene sets with matched mean-variance patterns. First, genes were grouped into 10 bins based on their mean expression, and into 10 (separate) bins based on their variance of expression across all cells. Given a list of genes (e.g., genes in a program), a cell-specific signature score was computed for each cell as follows: First, 1,000 random gene lists were generated, where each instance of a random gene-list was generated by sampling (with replacement) for each gene in the gene-list a gene from the equivalent mean and variance bin it was placed in. Then, the sum of centered and scaled gene expression in the given cell was computed for all 1000 random gene-lists generated and the z-score of the original gene-list for the generated 1,000 sample distribution is returned, as in (Singer et al., 2017).

Another program of highly correlated genes identified by PAGODA showed no biological relevance based on gene annotation, but was associated with cells processed on specific dates, suggested they reflect a contamination or batch effect. We scored each cell for this program with the above described method for scoring cells for gene signatures. When testing for differential gene expression over tumor development (described below), we included this batch effect score as a covariate in the regression analysis to control for genes that are correlated with it.

To test if a program's expression changes over the course of tumor development, we estimated a linear model for each program and compared with a likelihood ratio test a full model: *program.activity* ~*detected genes* + *time point* to a reduced

model: *program.activity ~detected genes.* For the time point covariate, healthy lung was taken as reference. We corrected the likelihood ratio test p values for multiple hypotheses for the number of programs using the *p.adjust* function computing the false discovery rate in the *stats* package.

Dimensionality reduction using diffusion component analysis

Diffusion components were calculated on a gene expression matrix limited to genes from programs of interest: programs 1,4,5,14,15 and 21 for T_{conv}, and programs 1,3,6,8,9,12,13,18,21,23 and 26 for T_{reg}. Gene expression was scaled for T_{regs} only across all cells. Diffusion components were calculated using the DiffusionMap function from the *destiny* package in R (Angerer et al., 2016) with a *k* of 30 and a local sigma. Significant diffusion components identified by the elbow in the eigenvalues were further used for dimensionality reduction to two dimensions. The eigenvectors of the significant diffusion components were imported into gephi 0.9.2 and a force directed layout using forceatlas 2 was run until it converged to get a two dimensional embedding.

Testing for differential gene expression during tumor development

To test whether individual genes change in gene expression over the course of tumor growth, we performed a two-step regression analysis. We focused on the proportion of cells expressing a gene, and hence on logistic regression. We performed logistic regression using the bayesglm function from the *arm* package in R. Because gender is often confounded with a particular time point in our experiment, we did not include it as a covariate in the model, but did remove all Y chromosome genes from analysis. We also excluded all genes expressed in > 95% or < 5% of cells in each mouse. We ran the logistic regression with expression data binarized at a log2(TPM+1) of 2 and using the following full model: *gene expression ~genes detected + batch effect + week p.i.* (healthy lung as reference) versus a reduced model: *gene expression ~genes detected + batch effect*. We identified a threshold for significance by the elbow method, identifying the peak of the second derivative of the ordered fdr distribution of the likelihood ratio test for each time point. To remove significant genes whose signal was driven by only one mouse, we performed another logistic regression using a mixed effect model, accounting for mouse variability: To this end, we added to the significant genes 1,000 randomly selected genes that were non-significant by the initial test to serve as background genes, and performed a mixed effect logistic regression using the glmer function of the lme4 package in R, with the model *gene expression ~tmp + (1|mouse)*, allowing the intercept to vary by mouse. We combined the elbow method above and the background genes to select an FDR cutoff for significance of 0.01. A gene was classified as significantly varying during tumor development if it passed this FDR cutoff in at least one time point.

T cell receptor (TCR) reconstruction and clonotype calling

TCR were reconstructed using Tracer (Stubbington et al., 2016), run in short read mode with the following settings '–inchworm_only = T–trinity_kmer_length = 17'. To call shared clonotypes between T_{reg} and T_{conv} cells, we required all cells of a clone to have identical productive TCRA and TCRB.

Comparison of bulk and scRNA-seq signatures to published signatures

Lists of differentially expressed genes in human cancer T_{regs}, mouse tissue T_{regs}, Tr17 cells from mice, and mouse activated T_{regs} (Table S4) were collected either from the supplementary tables of the relevant publications, or generously provided by the authors upon request (De Simone et al., 2016; Guo et al., 2018; Kim et al., 2017; Magnuson et al., 2018; Miragaia et al., 2019; Plitas et al., 2016; Tan et al., 2016; Zheng et al., 2017).

ST2 transcriptional programs in human colorectal cancer T_{regs}

To examine the generalizability of our findings and their relevance to human cancer, we identified gene programs that co-vary with ST2 expression in human colorectal cancer T_{regs} (Zhang et al., 2018). We compared cells in which ST2 was detected ($ST2^+$) and cells in which ST2 was not detected ($ST2^-$) to identify an $ST2^+$ program. Differential expression analysis was performed using t test on the log-transformed TPM values. We confirmed that the program was not confounded by cell quality and ensured that it captured differences between $ST2^+$ and $ST2^-$ cells within each tumor (data not shown). To this end, we first computed the overall expression (OE) of the program across the relevant T cells, in a way that eliminates technical noise, as previously described (Jerby-Arnon et al., 2018). We then tested whether the OE of the program was higher in $ST2^+$ cells compared to ST2- by using a mix-effected multilevel (random intercepts) regression model, where the program OE is the dependent variable and ST2 detection is provided as a binary covariate. The model included patient-specific intercepts to control for the dependency between the scRNA-seq profiles of cells from the same tumor, and controlled for cell complexity with a covariate that denotes the number of genes detected in each cell. The model was implemented using the lme4 and lmerTest R packages (https://cran.r-project.org/web/packages/lme4/index.html).

Processing and analysis of droplet-based scRNA-seq

De-multiplexing, alignment to the mm10 transcriptome and unique molecular identifier (UMI)-collapsing were performed using the Cellranger toolkit from 10X Genomics version 1.1.0. For each cell, we quantified the number of genes for which at least one read was mapped, and then excluded all cells with fewer than 500 detected genes. Genes that were detected in less than 3 cells were excluded. Expression values $E_{i,j}$ for gene *i* in cell *j* were calculated by dividing UMI counts for gene *i* by the sum of the UMI counts

in cell *j*, to normalize for differences in coverage, and then multiplying by 10,000 to create TPM-like values (TP10K), and finally computing $\log_2$(TP10K + 1).

Selection of variable genes was performed by fitting a logistic regression to the cellular detection fraction (often referred to as α), using the total number of UMIs per gene as a predictor (Montoro et al., 2018). Outliers from this curve are genes that are expressed in a lower fraction of cells than would be expected given the total number of UMIs mapping to that gene, that is, likely cell-type or state-specific genes. We used a threshold of deviance of < -0.15 and a minimum of 100 total UMIs. We restricted the expression matrix to this subset of variable genes and values were centered and scaled and capped at a z-score of 10.

We restricted the expression matrix to the subsets of variable genes and high-quality cells noted above, and then centered and scaled values before inputting them into principal component analysis (PCA), implemented using 'RunPCA' in Seurat which runs the irlba function. After PCA, significant principal components were identified using the elbow-method when looking at the distribution of singular values. Scores from only those significant principal components were used as the input to further analysis. For visualization purposes, the dimensionality of the datasets was further reduced to 2D embeddings using the RunUMAP() function on the first 24 PCs and clusters were identified using the FindNeighbors() and FindClusters() functions of the *Seurat* package in R. Clusters were post hoc merged to six major cell populations using canonical markers for all cell types detected.

Analysis of IHC Images

QuPath software was used to annotate tumor and lobe areas (Bankhead et al., 2017). CD8-stained and Foxp3-stained images were standardized to a common set of stain vector parameters. $CD8^+$ cell detection was performed using the PositiveCellDetection plugin with the following parameters:

runPlugin('qupath.imagej.detect.nuclei.PositiveCellDetection', '{"detectionImageBrightfield": "Optical density sum," "requestedPixelSizeMicrons": 0.5, "backgroundRadiusMicrons": 8.0, "medianRadiusMicrons": 0.0, "sigmaMicrons": 1.5, "minAreaMicrons": 7.0, "maxAreaMicrons": 125.0, "threshold": 0.3, "maxBackground": 2.0, "watershedPostProcess": true, "excludeDAB": false, "cellExpansionMicrons": 2.0, "includeNuclei": false, "smoothBoundaries": false, "makeMeasurements": true, "thresholdCompartment": "Cytoplasm: DAB OD max," "thresholdPositive1": 0.7, "thresholdPositive2": 0.4, "thresholdPositive3": 0.6, "singleThreshold": true}');

$Foxp3^+$ cell detection was performed using the PositiveCellDetection plugin with the following parameters:

runPlugin('qupath.imagej.detect.nuclei.PositiveCellDetection', '{"detectionImageBrightfield": "Optical density sum," "requestedPixelSizeMicrons": 0.5, "backgroundRadiusMicrons": 8.0, "medianRadiusMicrons": 0.0, "sigmaMicrons": 1.5, "minAreaMicrons": 7.0, "maxAreaMicrons": 125.0, "threshold": 0.3, "maxBackground": 2.0, "watershedPostProcess": true, "excludeDAB": false, "cellExpansionMicrons": 2.0, "includeNuclei": false, "smoothBoundaries": false, "makeMeasurements": true, "thresholdCompartment": "Cell: DAB OD mean," "thresholdPositive1": 0.3, "thresholdPositive2": 0.4, "thresholdPositive3": 0.6, "singleThreshold": true}');

Scored cells were normalized to tumor area.

Additional statistical analyses

Unpaired, two-tailed Student's t tests, Mann-Whitney tests, Tukey's multiple comparisons tests, and Sidak's multiple comparisons tests were used for all statistical comparisons using GraphPad Prism software.

DATA AND CODE AVAILABILITY

The accession number for the bulk and scRNA-Seq data reported in this paper is GEO: GSE139232. All code is available upon request.